Catalysis Science & Technology

ROYAL SOCIETY OF CHEMISTRY

PAPER

View Article Online
View Journal | View Issue

Cite this: *Catal. Sci. Technol.*, 2025, 15, 6161

Permanent free radicals in bamboo biochar-based flow bed reactor: a sustainable solution for dye degradation *via* adsorption and radical oxidation

Paola Franchi,[a] Anna Turchetti, [a] Marco Lucarini, [a] Adolfo Manucci,[b] Marcello Pagliero, [b] Antonio Comite,[b] Alessandro Pellis, [b] Letizia Savio, [c] Elina Mkrtchian,[c] Giorgio Divitini, [d] Ambra Celotto,[d] Sergio Marras,[d] Tommaso Del Rosso, [e] Sidnei Paciornik, [f] Silvana Alfei [g] and Omar Ginoble Pandoli [*cdgh]

This study investigates the generation of hydroxyl radicals (•OH) using the biochar-packed column flow system for methylene blue (MB) degradation in the presence of oxygen. Electron paramagnetic resonance (EPR) was employed to quantify and analyse the stability of carbon-centred permanent free radicals (PFRs) in the solid state (10^{17}–10^{19} spins per g). In water, PFRs act as catalysts for the generation of hydroxyl radicals (•OH), which are responsible for the advanced oxidation process (AOP) of organic molecules. Bamboo-based activated carbons (BACs) were produced through fast pyrolysis at various temperatures ranging from 300 to 800 °C, with the gas environment switched from N_2 to CO_2. The BAC treated at 400 °C (B400), which balanced physicochemical properties (lower surface area, larger micropore volume, and higher formation of reactive oxygen species in water), demonstrated the highest performance in removing MB compared to B500 and B600. The efficiency of MB removal depended on the presence of •OH in aerated or purged solutions, and the crucial role of dissolved oxygen in the formation of •OH was established. Additionally, the study explores the kinetics of MB removal, emphasising the predominance of chemical mechanisms such as electron transfer reactions and PFR-mediated oxidative degradation. This work provides valuable insights into the potential application of BACs for environmental remediation, particularly in treating dye-contaminated wastewater, eliminating the need to add H_2O_2 as a chemical source of reactive oxygen species (ROS) in solution.

Received 26th May 2025,
Accepted 25th August 2025

DOI: 10.1039/d5cy00632e

rsc.li/catalysis

1. Introduction

The increasing demand for effective wastewater treatment solutions has significantly impacted the time and cost of producing biosorbent materials derived from biomass. Among these materials, carbon-based catalysts have garnered considerable attention due to their exceptional properties, including high surface area, tuneable porosity, and excellent thermal and chemical stability. Chemically and physically activated carbon (AC) has been identified as a promising candidate for water treatment applications, both in batch and flow setups.

Bamboo-based activated carbons (BACs) offer a sustainable and effective alternative to other sources of AC, such as coconut shells, wood, and peat. Bamboo is a highly renewable resource, growing rapidly and sustainably.[1] It can be harvested without causing significant environmental damage, making it an eco-friendly option for activated carbon production. While coconut shells and wood are also renewable, their growth rates and environmental impacts greatly vary. On the contrary, peat is less sustainable, due to the slow regeneration of peatlands.[2] BAC has several unique properties and advantages. Its high porosity, adsorption capacity, and environmental benefits make it a valuable material for various applications.[1] The activation process

[a] *Department of Chemistry "Giacomo Ciamician", Via P. Gobetti 85, 40129, Bologna, Italy*
[b] *Department of Chemistry and Industrial Chemistry, University of Genoa, Via Dodecaneso, 31, 16146, Genoa, Italy*
[c] *Istituto dei Materiali per l'Elettronica e il Magnetismo del Consiglio Nazionale delle Ricerche, UOS Genova, Via Dodecaneso 33, Genova, Italy*
[d] *Istituto Italiano di Tecnologia (IIT), Via Morego 30, 16163, Genova, Italy. E-mail: omar.ginoble@iit.it*
[e] *Departamento de Fisica, Pontifícia Universidade Católica, Rua Marques de São Vicente, 225, 22451-900, Rio de Janeiro, Brazil*
[f] *Departamento de Engenharia Química e de Materiais, Pontifícia Universidade Católica, Rua Marques de São Vicente, 225, 22451-900, Rio de Janeiro, Brazil*
[g] *Department of Pharmacy, University of Genoa, Viale Cembrano, 4, 16148 Genoa, Italy. E-mail: omar.ginoblepandoli@unige.it*
[h] *Departamento de Química, Pontifícia Universidade Católica, Rua Marquês de São Vicente, 225, 22451-900, Rio de Janeiro, Brazil. E-mail: omarpandoli@puc-rio.br*

(chemical or physical) further increases its porosity and adds chemical functional groups, making it even more effective for several environmental applications. BAC with a high surface area and small pores is suitable for adsorbing volatile organic compounds (VOCs) and gases for air purification, or heavy metals for water decontamination. Conversely, smaller surface areas and larger pores are suitable for adsorbing larger organic compounds for water remediation. Even though these carbonaceous materials have gained attention for environmental applications, it is worth noting the environmental impact of the PFR present in the biochar, considered a new class of pollutants given their reactivity with O_2 and water to form dangerous ROS.[3–5]

The feedstock biomass, the thermal treatment, and the biochar's pre-, *in situ*, and post-treatment can influence the formation of carbon- or oxygen-centred PFR in lignocellulosic-derived biochar. The daily or monthly long-life stability of PFRs is determined by the resonance delocalisation of the radical over the aromatic structure of the graphite carbon, while their passivation can occur with atmospheric oxygen, or the ROS self-generated in the solution.[6–8]

The biochar's environmental applications as bio-adsorbent[9,10] for industrial wastewater treatment, and remediation of organic[11] and pharmaceutical[12] pollutants in water are well demonstrated. Studies proved the biochar's absorption capacity and the pivotal role of its PFRs in the degradation of contaminants in batch-mode experiments.[13] However, the research on biochar's implications as an electroactive donor, acceptor and mediator involving redox reactions[14] and advanced oxidation process (AOP)[15–17] is still embryonic. Correctly measuring and tuning the electrochemical properties of biochar, such as electron exchange capacity (EEC), electrical conductivity and superficial electroactivity, is still a scientific debate.[18–20] The implications of EEC of PFRs for storing and shuttling electrons to break down contaminants have recently been reviewed.[21] New attention has been given to the electroactive biochar (e-biochar) used as carbon-based electrodes for capacitive flow water desalination[22] and microbial electrochemical technologies (MET).[23] Klüpfel *et al.* have demonstrated the electron-donating capacity and electron-accepting capacity of plant-derived biochar depending on the heat treatment temperature.[24] Fang *et al.* proposed a three-step mechanism, where single-electrons transfers are involved in the hydroxyl radical ($^{\bullet}OH$) formation from biochar in suspension: i) first, PFRs act as electron donors and transfer one electron to molecular oxygen to form the ROS superoxide anion ($O_2 + e^- \rightarrow O_2^{\bullet-}$); ii) PFRs catalyse the dismutation of superoxide anion adding another electron to produce hydrogen peroxide and oxygen ($2O_2^{\bullet-} + e^- + 2H^+ \rightarrow H_2O_2 + O_2$); iii) finally, PFRs donate a single electron to hydrogen peroxide to generate hydroxyl radical ($H_2O_2 + e^- \rightarrow {}^{\bullet}OH + {}^{-}OH$).[25]

Our previous work highlighted the tandem process of adsorption followed by an oxidative radical process of MB mediated by $^{\bullet}OH$ with H_2O_2 into a bamboo-based biochar-packed flow system. The biochar's PFRs obtained in slow pyrolysis in N_2, without chemical or physical treatments, played a fundamental role in activating H_2O_2 and generating $^{\bullet}OH$.[26]

In the present study, the BAC is obtained by fast pyrolysis in a N_2 atmosphere and subsequently activated with CO_2 to enhance its adsorption capacity. An unexpected $^{\bullet}OH$ mechanism generation was discovered, promoted by dissolving molecular oxygen in water. The MB removal process occurs by adsorption and oxidation mechanisms facilitated by structural morphology and the existence of PFRs in the BAC, respectively. Using the EPR technique, the stability of PFRs (10^{17}–10^{19} spins per g) in the solid state was monitored for five months, while the EPR spin-trapping method identified the PFRs' role in hydroxyl radical generation in aerated water, in batch and flow-mode, without adding H_2O_2. This approach eliminates the need for adding H_2O_2 (ref. 27) or (Fe^{2+})[28] as a chemical source of $^{\bullet}OH$ in solution, thereby catalysing the oxidative degradation of MB.

2. Experimental section, materials and methods

2.1 Sample preparation and characterisation

Untreated bamboo *Dendrocalamus giganteus* blocks of 4 cm^3 were washed twice with warm water (60 °C) for 1 hour, and dried overnight in the oven at 90 °C until a constant weight was reached. They were placed in a horizontal fixed bed under an N_2 flow of 100 ml min^{-1}, reaching a temperature range from 300 to 800 °C in fast pyrolysis (10 °C min^{-1}). Once the maximum temperature was reached, the gas was switched to CO_2, maintaining the temperature for 1 hour. The samples were cooled at 5 °C min^{-1} till 200 °C and were then left to cool to room temperature. The BAC material was pulverised in a ball-milling system (Recth model) for 5 or 20 minutes and stored under N_2 until its use. Our previous works used a similar procedure in slow pyrolysis in N_2 atmosphere, without the exposure to CO_2.[26,29,30]

To determine the chemical and physical evolution of the lignocellulose biomass, BAC powders were characterised by Attenuated Total Reflectance-Fourier Transform Infrared Spectroscopy (ATR-FT-IR) and Diffusion Reflectance Infrared Fourier Transform Spectroscopy (DRIFTS), Raman Spectroscopy (RS), electron paramagnetic resonance (EPR), and Scanning Electron Microscopy-Energy Dispersive X-ray Spectroscopy (SEM/EDX). BAC slices were investigated by X-ray diffraction (XRD), and X-ray photoemission spectroscopy (XPS) analysis.

ATR-FT-IR and DRIFTS (Vertex 70, Bruker Optics) were employed in the 4000–400 cm^{-1} range with 128 scans and 2 cm^{-1} spectral resolution. Raman spectra were acquired by Raman Model Renishaw inVia with a laser excitation of 688 nm, a range acquisition of 500–2000 cm^{-1}, with 1 s exposure and 5 accumulations.

Nitrogen adsorption and desorption isotherms were measured by thermosetting the specimen in liquid nitrogen (−196 °C) using an Accelerated Surface Area and Porosity instrument (ASAP2020 MP Plus – Micromeritics, USA). An amount of each sample was carefully weighed in a testing tube and degassed under vacuum at 180 °C for 8 hours. The specific surface area was determined by the Brunauer–Emmett–Teller (BET) method, while the pore volume was calculated using the *t*-plot method for micropores, the Barrett–Joyner–Halenda (BJH) for mesopores and by the single point method at a relative pressure of 0.99 for the total pore volume. The cumulative pore volume was obtained using a density functional theory method (DFT).

X-ray diffraction analysis on BAC slices was performed on a Malvern-PANalytical 3rd generation Empyrean X-ray powder diffractometer. The instrument was equipped with a 1.8 kW CuKα ceramic X-ray tube operating at 45 kV and 40 mA, iCore and dCore automated PreFIX optical modules and solid-state hybrid pixel PIXcel3D operating in 1D mode. The XRD patterns were collected from 5° to 90° with a step size of 0.052° in Bragg–Brentano geometry. The acquisition was carried out in air at room temperature.

The surface chemical composition of BAC was investigated by X-ray photoemission spectroscopy using a hemispherical analyser model 10-360 and a monochromatic X-ray source model 10-610 by Physical Electronics. The instrument is hosted in an ultra-high vacuum (UHV) chamber with a base pressure better than 5×10^{-8} mbar and a load-lock system for fast sample entry. XPS spectra were acquired using monochromatized $Al_{K\alpha}$ photons of energy $h\nu$ = 1486.6 eV; photoemitted electrons were collected from a spot of approximately 100 μm diameter. XPS spectra were analysed using the KolXPD software. According to the literature, the binding energies (E_b) were calibrated by setting the maximum of the C 1s line to 284.5 eV.[30–34] The C 1s was fitted using three Voigt functions and a Shirley background at 300 °C, while a Doniach–Sunjic convoluted with a Gaussian plus two Voigts were necessary to reproduce the experimental data for pyrolysis at $T \geq 400$ °C. The O 1s region was fitted using three Voight functions after subtracting a Shirley background, while up to two Voigt functions and a linear background were used for the N 1s region. Peak areas are affected by an error of ±5% for the C 1s and ±7% for the smaller O 1s signals. For a quantitative evaluation of the relative elemental concentration, the fitted C 1s and O 1s areas must be weighted with respect to the corresponding atomic sensitivity factor (ASF – considering the photoemission cross section and the transmission function of the analyser).[34]

Scanning Electron Microscopy was carried out in a ZEISS GeminiSEM 560 equipped with a Gemini 3 column and an Oxford Instruments EDX detector. The acceleration voltage was set to 5 kV for imaging and 20 kV for spectroscopy. The samples were dispersed on carbon tape.

2.2 Permanent free radicals (PFRs) at solid-state and transient radical oxygen species determination by EPR spectroscopy

Electron paramagnetic resonance (EPR) spectra were recorded by Bruker ELEXSYS E500 spectrometer equipped with an NMR Gaussmeter for the calibration of the magnetic field and a frequency counter for the determination of *g*-factors. The powders of different bamboo-activated carbon were weighed directly (*ca.* 5–10 mg) into glass capillaries, sealed at the bottom, placed inside EPR tubes, accurately positioned inside the cavity, and the analysis of the solids was carried out at room temperature. Measurement conditions: modulation amplitude = 1.0 G; conversion time = 81.92 ms; time constant = 81.92 ms; modulation frequency = 100 kHz; field width = 100 G, microwave power = 0.80 mW; and microwave frequency = 9.30 GHz. Measured *g*-factors were corrected with respect to that of a standard sample of a perylene radical in concentrated H_2SO_4 (g = 2.0026) and checked against the measured value for 2,2-diphenyl-1-picrylhydrazyl radical (DPPH) at the solid state (g = 2.0036). The concentration of radicals present in the BACs powders, not exposed to atmospheric oxygen, was monitored for five months comparing the double integral of the EPR signal with that of a reference solution of tetramethyl piperidin-*N*-oxyl radical (TEMPO, Sigma-Aldrich) in an inert solvent such as hexane, using the signal from a piece of synthetic ruby fixed to the inside wall of the microwave cavity as a sensitive reference.

A spin-trap EPR technique, coupled with 5,5-dimethyl-1-pyrroline-*N*-oxide (DMPO, Sigma Aldrich, cat. no. 92688) as a spin-trapping agent, was used to detect hydroxyl radical ($^{\bullet}OH$, a short-lived radical paramagnetic species) generated from BAC suspension (batch mode) or from BAC deposited into a filter or packed into the chromatographic column (flow mode). The generation of $^{\bullet}OH$ was detected by the four-line EPR spectra (1 : 2 : 2 : 1) corresponding to the stable paramagnetic species DMPO$^{\bullet}$–OH, a long-lived spin adduct, formed by the reaction of $^{\bullet}OH$ with DMPO ($a_N = a_H$ = 14.84 G).[26] The first series of analyses was conducted by percolating 500 μL of a diluted H_2O_2 solution (2.68 mM), passed through a sintered funnel containing 20 mg of different BAC powders, into 500 μL of a 0.04 M solution of DMPO. The final concentration of DMPO was 0.02 M, and that of H_2O_2 was 1.34 mM. 20 μL of each mixed solution was introduced into a capillary tube and placed inside an EPR tube. The blank consists of 20 μL of DMPO (0.02 M) and H_2O_2 1.34 mM (Fig. 10).

The second series of analyses in batch was conducted by sonicating for 20 minutes at 37 °C two vials containing 2 mg of B400 powder suspended in 200 μL of a 0.1 M solution of DMPO in PBS 0.01 M (pH 7.4), purging N_2 (absence of dissolved O_2) or bubbling air (enriching O_2), respectively. After the solids settled, 20 μL of each supernatant was introduced into a capillary tube and placed inside an EPR tube. The third analysis series was conducted through a flow-bed packed reactor loaded with 10 mg of B400 and 5 g of

glass beads. 10 mL of distilled water (purged with air or N_2) was injected into the column at 0.25 mL min^{-1}, and each 0.250 mL percolated solution was recollected into the vials containing 0.250 mL of 0.04 M buffered solution of DMPO for 10 minutes (Table 10 and Fig. 14).

2.3 Column-packed flow systems for MB removal

Omnifit™ EZ chromatography columns with one fixed and one adjustable endpiece (Ø = 6.6 mm, 150 mm length) were used for the bed-packed flow experiments. Each column was filled with 5 g of SiLibeads® (100–200 μm or 150–250 μm, Avantor) and 10 or 100 mg of BAC (B400 and B500). Methylene blue (MB, CAS 61-73-4) from ISOFAR (Rio de Janeiro, Brazil) was used as an organic dye to probe the BAC's absorption capacity and long-term removal efficiency. A peristaltic pump (Ismatec-Cole Palmer) was connected to the BAC-packed column system and the MB solution was continuously pumped from a reservoir. In Table 1, the amounts of biochar packed into the columns, the concentration and the volumes of MB are summarized.

Two setups were used. In the first setup, 100–160 mL of MB solution (from 5 to 25 × 10^{-5} mol L^{-1}) was continuously injected at 0.5 mL min^{-1} flow rate into packed columns (10 and 100 mg of B400 or B500). 10–16 fractions (10 mL each) were subsequently collected in chromatographic glass tube and analysed by UV-vis spectrometer (Ocean Optics USB2000+) to determine the removal percentage % R of MB and the maximum adsorption capacity (Ads_{max}) of the activated carbon used. MB removal was monitored by Spectral Suite software (Ocean Optics), measuring the absorbance change at a fixed wavelength of 663 nm, and the R% was calculated using eqn (1):

$$\% R = \frac{[A_0 - A_t]}{A_0} \times 100 \quad (1)$$

where A_0 is the absorbance of the mother solution, and A_t is its absorbance after a time t flowing through the packed column. R% values were plotted *versus* fractions to obtain the MB cumulative removal efficiency (%) graph over number of the recollected volumes (fractions).

The maximum adsorption capacity (Ads_{max}) was calculated as mass of organic dye adsorbed per mass unit of BAC (mg_{dye} $g_{biochar}^{-1}$), using the eqn (2):

$$Ads_{max} = (C_0 - C_t) \times V \times MW_{MB}/m = [mg_{dye}\ g_{BAC}^{-1}] \quad (2)$$

where Ads_{max} is the mass adsorbed per mass unit of BAC (mg_{dye} g_{BAC}^{-1}), C_0 is the initial concentration of the organic dye, C_t is the measured concentration in each fraction, V is the volume of the solution collected, MW is the molecular weight of the organic dye, and m is the mass of the BAC used.

To investigate the role of dissolved molecular oxygen in forming $^{\bullet}OH$, the removal of MB was monitored using aged B400, with He and air purged in the organic dye solution. Into the reservoir the MB solution was continuously bubbling He or air with intent to decrease and increase the content of dissolved O_2, respectively.

In the second set-up, for the long-term removal efficiency test, 10 mL of MB solution (2.5 × 10^{-5} mol L^{-1}) was recirculated for 2 hours at 0.5 mL min^{-1} flow rate. At 30-, 60- and 120-minutes intervals the MB removal was monitored by UV spectrometry using eqn (1). The column was reused daily with fresh solutions up to 3 experiments (3 cycles per day). To assess the long-term efficiency of BAC, the packed column was used for a total of 12 cycles for 4 days to obtain the MB cumulative removal efficiency (%) graph *versus* number of cycles. For the sake of comparison, the long-term removal stability test was carried out with B400, B400-H_2O_2 and B400-N_2. The labelled sample B400-H_2O_2 was produced by adding 100 μL H_2O_2 (0.125 M) to 10 mL of MB (2.5 × 10^{-5} mol L^{-1}), with a molar ratio MB/H_2O_2 = 1/50. For the material labelled B400-N_2 we used a not-activated carbon pyrolyzed only with N_2-gas, as described previously.[26] To ensure the measurement's accuracy, each MB removal test in the flow-packed system was repeated in triplicate.

2.4 Kinetic study

Kinetic studies were carried out on the most significant data of removal efficiency (%) of B400 over time, by fitting them with the mathematical kinetic models reported in Table 2. Table 2 also reports their equations and the measures that must be reported on the x and y axes to obtain the related dispersion graphs.

A series of dispersion graphs were obtained and their linear regression models with related coefficients of determination R square (R^2) were provided by Microsoft 365 Excel software. The value of R^2 was the parameter used to select the mathematical model which best fitted the data of removal efficiency loss (%) over time and to assess the kinetics and mechanisms governing the loss of removal efficiency over time.[35]

Table 1 Experimental set-up for MB removal efficiency of two BAC (B400 and B500) varying concentration and volume of the organic dye, amounts of the BACs, and the injection flow mode

MB [mol L^{-1}] and volume	B400 [mg]	B500 [mg]	SiLibeads® support	Experimental set-up	
[25 × 10^{-5}] 100 mL	100	100	~150 μm	Continuous flow	Fig. 11a
[5.0 × 10^{-5}] 160 mL or 100 mL	100 or 10	100 or 10	~150 μm	Continuous flow	Fig. 11b and c
[5.0 × 10^{-5}] 100 mL	10	10	~200 μm	Continuous flow	Fig. 11d
[2.5 × 10^{-5}] 10 mL × 12 times	10	—	~200 μm	Recycling test for long-term removal stability	Fig. 12

Table 2 Variables to be reported on the *x* and *y* axes to obtain the dispersion graphs of mathematical models considered in this study and the equations expressing them

Model	*X* axis	*Y* axis	Equation
FO	Times	$\ln[\%\ R_{(t)}/\%\ R_{(t0)}]$	$\ln[\%\ R_{(t)}/\%\ R_{(t0)}] = -(K_1/2.303) \times t$
PFO	Times	$\ln[-(\%\ R_{(20h)} - \%\ R_{(t)})]$	$\ln[-(\%\ R_{(20h)} - \%\ R_{(t)})] = \ln \%\ R_{(20h)} - (K_1/2.303) \times t$
PSO	Times	$T/\%\ R_{(t)}$	$T/\%\ R_{(t)} = (1/\%\ R_{(20h)}) \times t + 1/[K_{PSO} + (\%\ R_{(20h)})^2]$
IPD	SRT[a]	$\%\ R_{(t)}$	$\%\ R_{(t)} = K_{IPD} \times t^{1/2}$
ELO	ln (times)	$\%\ R_{(t)}$	$\%\ R_{(t)} = \beta \times \ln(\alpha\beta) + \ln(t)$
KMP	ln (times)	$\ln(\%\ R_{(t)})$	$\ln[\%\ R_{(t)}] = n_{KP} \times \ln(t) + \ln(K_{KP})$

% *R* = removal percentage; FO = first order; PSO = pseudo first order; PSO = pseudo second order; IPD = intra particle diffusion; ELO = Elovich; KMP = Korsmeyer–Peppas. [a] Square root of times. $\%\ R_{(t)}$ is the removal percentage on time *t*; $\%\ R_{(20h)}$ is the residual removal percentage after 20-hours working in continuous flux; K_1 are the first-order or PFO constants; K_{PSO} is the equilibrium constant rate of the PSO kinetic model; K_{KP} is the transport constant of the Korsmeyer–Peppas model; n_{KP} (also called diffusional or transport exponent) provides information on the possible mechanism(s) governing the process under study; K_{IPD} is the intra particle diffusion constant; *I* = intercept.

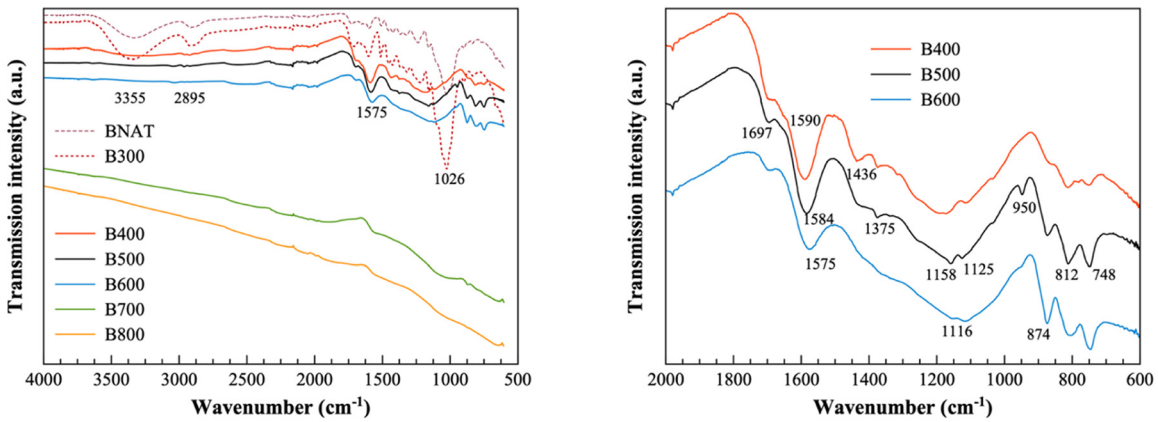

Fig. 1 ATR-FT-IR analysis of natural bamboo (BNAT) and pyrolyzed samples B300–B800 (left panel). Magnification of ATR-FT-IR spectra of B400, B500 and B600 (right panel) in the 600–2000 cm^{-1} region. In the images only the most representative bands are indicated.

3. Results and discussion

3.1 Chemical and physical characterisation of bamboo-derived carbon at the solid state

Chemical evolution of pyrolyzed biomass has been monitored by IR, XPS, Raman, and EPR techniques. The vibrational spectroscopy was suitable to observe the transformation of lignocellulose biomass during the torrefaction (300 °C) and the graphitization (400–800 °C) processes. The ATR-FT-IR spectra of BACs are presented in Fig. 1, and the complete band assignment is summarized in Table 3.

There is a clear difference between the three groups of biochar. B300, derived from lower temperature treatment, presents an FT-IR spectrum like that of natural bamboo (BNAT) raw material, indicating an irrelevant chemical modification during the torrefaction process. Specifically, predominant bands are observable, related to the stretching of aliphatic and aromatic hydroxyl groups at 3355 cm^{-1} and the symmetric and asymmetric bands of stretching C_{sp^3}–H at 2895 cm^{-1}. A diagnostic band at 1026 cm^{-1} is instead related to the (C–O–C) $\beta_{1\rightarrow4}$ glycosidic bond stretching of cellulose and hemicellulose. As observable in Fig. 1 and Table 3, as well as in Fig. 2 and Table 4, FT-IR and DRIFTS spectra present substantial differences between B400, B500 and B600, where the thermal treatment was relevant for the decomposition of hemicellulose, cellulose and lignin. Finally, for B700 and B800 all the vibration bands disappeared, indicative of the total degradation of the biomass during the graphitisation process at high temperature.

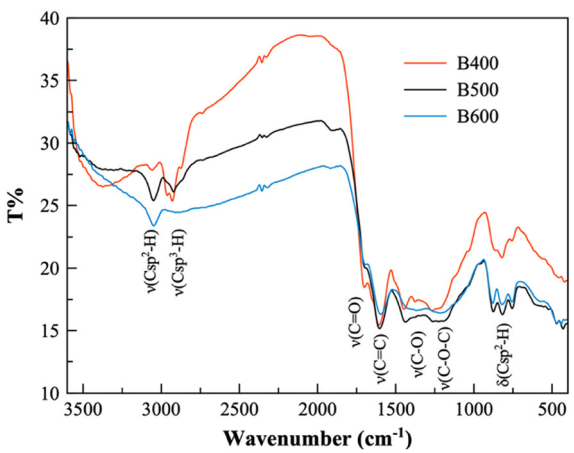

Fig. 2 DRIFTS analysis of pyrolyzed samples B400–B600.

Table 3 ATR-FT-IR frequencies and band assignments for natural bamboo (BNAT) and the pyrolyzed bamboo samples

Samples	Frequency (cm^{-1})	Characteristic vibration and functional group[a]
BNAT–B300	3355	ν(O–H) aromatic and aliphatic hydroxyl group
BNAT–B300	2895	Aliphatic $\nu(C_{sp^3}–H)$
BNAT–B300	1738	Aromatic carbonyl ν(C═O) of lignin and hemicellulose
BNAT–B300	1600–1505–1425	ν(C═C) of aromatic skeletal vibration
BNAT–B300	1026	ν(C–O–C) $\beta_{1\rightarrow4}$ glycosidic bond of cellulose and hemicellulose
B400	1437	δ_{ip}(O–H)
B400–B500–B600	1697	ν(C═O) carboxylic, phenolic ester and lactones groups
B400–B500–B600	1590–1584–1575 (respectively)	Aromatic ring ν(C═C) in lignin or conjugated ν(C–O)
B400–B500–B600	1158–1116 broad band	Aromatic and saturated ν(C–O) and residual ν(C–O–C) of ester groups in cellulose and hemicellulose
B400–B500–B600	1225–950 (several)	δ_{ip}(C–H) aromatic C–H in-plane bend
B400–B500–B600	874–812–748	δ_{oop}(C–H) aromatic C–H out-of-plane bend

[a] The vibration band were attributed following several ref. 35–40.

With more details, DRIFTS spectra (Fig. 2 and Table 4) allow us to follow the evolution of BACs' functionalities during the graphitization process. B400, when compared to B500 and B600, showed an abundance of cellulose and hemicellulose's functionalities stretching, such as –OH (3380 cm^{-1}), C_{sp^3}–H (2965–2871 cm^{-1}), and C═O (1701 cm^{-1}). The increased temperature during the graphitization of the BACs leads to chemical transformation of above polymers with an increment of aromatic ═C_{sp^2}–H stretching and bending, at 3048 and 880–817–755 cm^{-1}, respectively. With the progress of the pyrolysis the intensity of O–H vibration decreases. The frequency at 1701 cm^{-1}, attributed at the stretching of (C═O) carboxylic and ester groups of the hemicellulose, disappeared, while the C═C vibration shifted to a lower frequency, from 1608 to 1598 cm^{-1}, for an increasing of the conjugation during the aromatisation process. The three bands at 880–817–755 cm^{-1} were attributed to the aromatic group's (═C–H) bending out-of-plane.

Raman spectra were recorded to monitor the pyrolytic evolution of BACs' carbon structure. They provide information about defects, order, and electronic characteristics of carbonaceous material. As shown in Fig. 3, all the samples presented two peaks: the D band at 1364–1330 cm^{-1} is associated to the disordered and distorted graphene layers of carbon material; the G-band at 1586 cm^{-1} is associated to the in-plane vibration of aromatic rings.

Table 5 shows that the G-band is stable at 1583 cm^{-1} for the samples B400, B500 and B600, while it slightly shifts to 1589 cm^{-1} in the higher graphitised samples, B700–B800.

On the contrary, the downshift of the D-band from 1364 to 1330 cm^{-1} is more significant and indicates an increase in the size of the carbon crystals. An increase in the intensity ratio I_D/I_G can be noticed, which can roughly indicate an increase in the disorder of the graphitic and turbostratic sheets, an observation that is supported by the literature.[30]

It is worth noting that with increasing thermal treatment, the fluorescence background disappeared, confirming that the first three samples still present auto-fluorescent lignocellulose polymers. The second group of samples, B700 and B800, did not present fluorescence, indicating the

Table 4 Diffuse Reflectance Infrared Fourier Transform Spectra (DRIFTS) vibration frequencies and band assignments for B400, B500 and B600

Samples	Frequency (cm^{-1})	Characteristic vibration and functional group[a]
B400	3380	ν(O–H) stretching of H-bonded phenolic and alcoholic –OH
B500–B600	3048↑	$\nu(C_{sp^2}–H)$ stretching of aromatic C–H
B400	2965–2925–2871↓	$\nu_{asym-sym}(C_{sp^3}–H)$ stretching of aliphatic C–H_x
B400–B500–B600	1701	ν(C═O) aromatic carbonyl/carboxylic groups, phenolic ester and lactones groups
B400–B500–B600	1608–1603–1598 (respectively)	ν(C═C) aromatic ring stretch, ν(C═O) stretching of conjugated ketones and chinones
B400–B500	1448–1438	$\delta_{asym}(C_{sp^3}–H)$ bending of aliphatic C–H_x
B400–B500	1376–1379	$\delta_{sym}(C_{sp^3}–H)$ bending of aliphatic C–H_x and δ_{ip}(O–H)
B400–B500	1270–1266	ν(C–C) skeletal vibration
B400–B500–B600	1250	ν(C–N) stretching vibration
B400–B500–B600	1200	ν(C–O) phenol stretching
B400–B500	1030–1031	ν(C–O–C) aliphatic ether and ν(C–O) alcohol stretching
B600	1515–950 Broad band	ν(C═C) aromatic ring stretching and $\delta(C–H)_{ip}$ aromatic in-plane bending, saturated ν(C–O) and residual ν(C–O–C)
B500–B600	880–817–755↑	$\delta(C–H)_{oop}$ aromatic C–H out-of-plane

[a] The vibration band were attributed following several ref. 36–41. ↑Downward arrow indicates a decrease of the band; ↓upward arrow indicates an increase of the band.

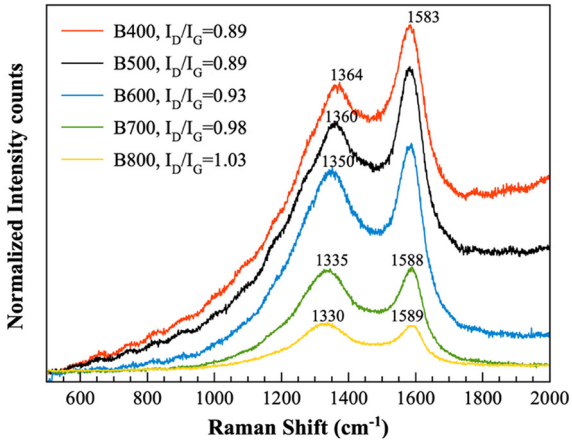

Fig. 3 Raman spectra of biochar B400–B800.

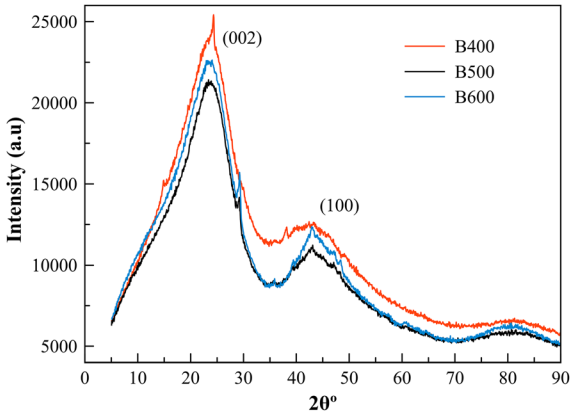

Fig. 4 XRD diffractograms of B400, B500 and B600.

Table 5 Raman shifts of the D and G-bands of the pyrolyzed samples B400–B800

	I_D/I_G	D-band (cm^{-1})	G-band (cm^{-1})
B400	0.89	1364	1583
B500	0.89	1369	1583
B600	0.93	1350	1583
B700	0.98	1335	1588
B800	1.03	1330	1589

completion of the chemical transformation of the polymer into graphite-like carbon.

The XRD patterns of the different pyrolyzed samples, shown in Fig. S1 and S2 (Section S1, SI), confirmed the ATR-FT-IR data. The torrefaction process at 300 °C did not determine a phase transformation of the lignocellulose biomass, showing diffraction peaks at 16° and 22° of the typical crystal planes of cellulose I.[30] The BAC produced at increased temperature from 400 to 700 °C showed a similar XRD pattern. The evolution of biomass's graphitisation from B300 to B400 produced an amorphous carbon material which demonstrated two main diffraction peaks around 23° and 43°, corresponding to (002) and (100) planes of graphitic-like faces, respectively. B800 proved the highest degree of graphitisation,[29] while B400 had the highest amorphous carbon content. Table 6 summarises the most important information extracted from the XRD pattern (Fig. 4). The (002) signal is attributed to the stacking of the graphene structure, while the (100) is attributed to the turbostratic carbons with distorted and not well-aligned graphene sheets. B400, compared to B500 and B600, presented the higher $d_{(002)}$- and $d_{(100)}$-spacing of 3.757 and 2.118 Å, respectively. This data will be relevant to consider the adsorption capacity of B400 inside the pore and the interlayered graphenic sheets.

Table 6 Data analysis of XRD patterns of pyrolyzed bamboo slice samples

Sample	2θ° (002)	FWHM (°) (002)	d-Spacing (Å) $d_{(002)}$	(2θ°) (100)	FWHM (°) (100)	d-Spacing (Å) $d_{(100)}$
B400	23.70	11.57	3.757	42.28	21.10	2.118
B500	24.01	11.01	3.704	43.28	14.72	2.089
B600	23.90	11.72	3.720	43.38	12.74	2.084

The thermal evolution of bamboo during fast pyrolysis was analysed using X-ray photoelectron spectroscopy to assess changes in oxygen and carbon content after treatment at temperatures ranging from 300 °C to 800 °C, as well as to determine the chemical transformations in the samples (Fig. 5).

The survey spectra recorded at various stages of the fast pyrolysis treatment are shown in Fig. 5. All spectra are dominated by the O 1s and C 1s lines, which appear at binding energies of approximately 532 eV and 285 eV, respectively. The relative intensity of these lines changes

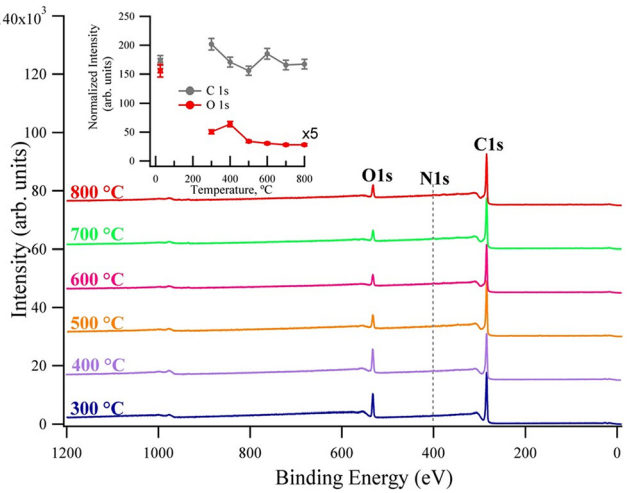

Fig. 5 Survey XPS spectra reporting the thermal evolution of bamboo from B300 °C up to B800 °C. The assignment of the main photoemission lines is indicated. Spectra are upshifted for the sake of clarity; inset: relative C 1s and O 1s intensity *vs.* *T*. The peak areas are normalized to the corresponding background; the level of carbon and oxygen of natural bamboo from previous work[30] is indicated by the arrows of the corresponding color pointing towards the vertical axis.

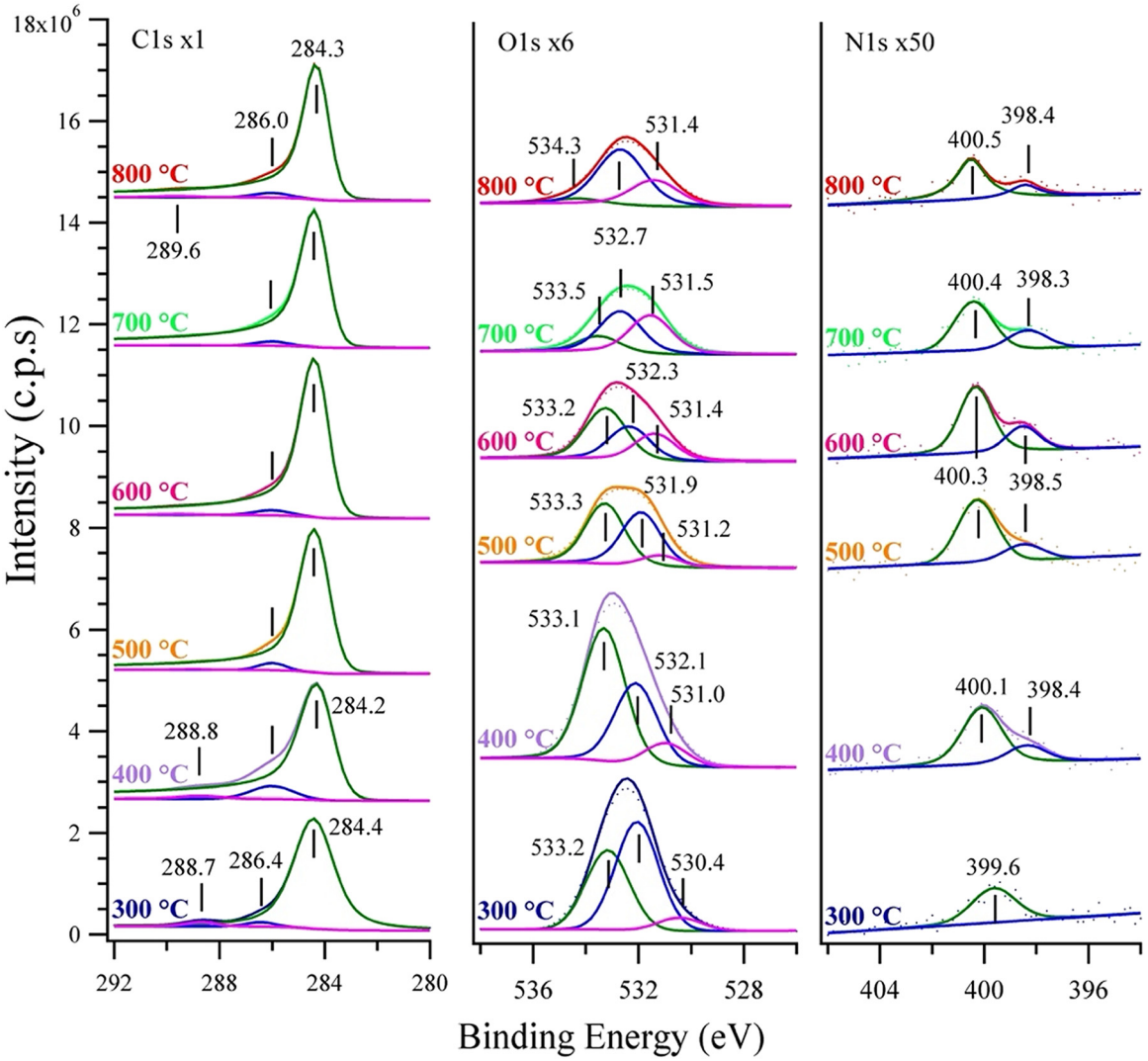

Fig. 6 High-resolution XPS spectra of the thermal evolution of bamboo samples from B300 up to B800. The outcome of the fitting procedure and the different components identified for each spectrum are reported. Spectra are normalised to the low E_b side of the B300 background and then upshifted for the sake of clarity. Please note the different enlargement factors for the three panels.

significantly during the fast pyrolysis process. The inset shows the total C 1s and O 1s intensity *vs.* pyrolysis temperature, together with the corresponding values previously measured for BNAT and reported for comparison. While the C 1s intensity decreases only slightly, the O 1s signal drops significantly with respect to BNAT already at 300 °C and decreases further at 500 °C, thus revealing de-oxygenation of the sample induced by the thermal treatment. The C/O ratio, calculated considering the different cross sections for the two photoelectrons, varies from ~5 at 300 °C to ~11 at 800 °C. These values are higher than those estimated for N_2-pyrolized bamboo,[30] indicating a more efficient deoxygenation in the present case. The N 1s peak intensity was negligible for all samples subject to fast pyrolysis treatment in the investigated temperature range. Fig. 6 shows the corresponding high-resolution XPS spectra of the C 1s, O 1s, and N 1s regions.

The C 1s region is characterised by a peak centred at E_b = 284.4 eV with additional minor components at E_b = 286.0 eV and E_b ~289 eV (left panel). They correspond to sp^2 C atoms involved in C–C, C–H bonds and the presence of residual C–N and C═O (carboxylate and carboxylic groups), respectively. For BNAT and early stages of pyrolysis, the bond

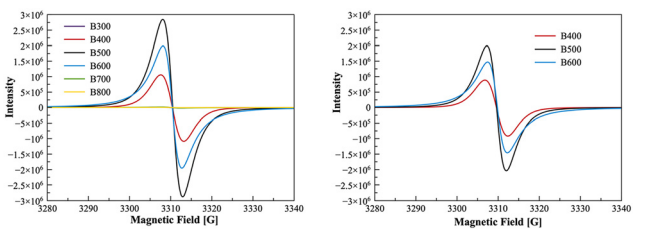

Fig. 7 (Left) EPR signals of all BAC powders stored for 3 months under N_2 at +4 °C. (Right) EPR signals stability BAC powders stored for 5 months.

Table 7 EPR parameters (spins per g, line width and *g*-factor) of stored BACs as the average of two analysis

Powders	*g*-Factor	PFR conc. [spins per g][a]	Line width	*g*-Factor	PFR conc. [spins per g]	Line width
BACs stored for 3 months under N_2 at +4 °C				BACs stored for 5 months		
B300	20 036	2.62×10^{17}	6.07	20 030	0.87×10^{19}	5.60
B400	20 029	1.24×10^{19}	5.70	20 029	2.12×10^{19}	4.69
B500	20 029	2.42×10^{19}	4.85	20 027	2.24×10^{19}	4.66
B600	20 027	2.44×10^{19}	4.92			
B700	20 028	8.85×10^{17}	4.86			
B800	20 028	1.60×10^{17}	5.50			

[a] TEMPO 3.5 mM in cyclohexane (*g*-factor = 2.0063) was used as an external standard. 15 μL were taken to have approximately the same volume of tube occupied by the powders.

at E_b = 284.4 eV primarily originated from lignin. On the contrary, bonds at E_b = 286.0 eV originated from cellulose, as mentioned in our previous work.[30] Changes in the intensity and shape of the peaks occurred with increasing temperature. Specifically, the C 1s peak at E_b = 284.4 eV became sharper and exhibited the typical asymmetry of graphite after pyrolysis at 400 °C, *i.e.* at a lower temperature than reported before.[30] Correspondingly, the higher energy peaks became negligible above 400 °C.

For the O 1s region, we observed a peak centred around 532.5 eV, which initially consisted of three components detectable at E_b = 530.4 eV (O1), 532.1 eV (O2), and 533.2 eV (O3). The O2 component corresponded to the O–C═O bonds initially present in lignin, while O3 can be assigned to the C–O bonds of cellulose.[32] With increasing pyrolysis temperature, their binding energy slightly upshifts, and their relative intensity changes significantly while the total intensity reduces. Indeed, while the small increases observed between 300 °C and 400 °C are within experimental error, the total O 1s signal decreases monotonously afterwards. In this evolution, the reduction of the component at E_b ~533.5 eV is largest between 400 °C and 600 °C, and such component becomes negligible at temperatures over 700 °C. Indeed, the changes in the O2 and O3 components during thermal evolution indicate that bamboo surface becomes richer in lignin and poorer in cellulose.[31]

The XPS spectrum of the N 1s region shows one distinct peak at E_b = 399.6 eV for the sample pyrolyzed at 300 °C related to imine groups (–C═NH). For higher temperatures, two types of N-groups can be identified on the BAC surface, a major component around 400 eV and a minor one around 398.4 eV, corresponding to nitrogen atoms in pyridinic and pyrrolic groups, respectively.[42,43]

The EPR technique was used to quantify the content of PFRs in the selected BAC at the solid state. Fig. 7 illustrates EPR spectra and the effect of the pyrolysis procedure on the PFRs concentration, radical characteristics and stability for 5 months. Table 7 and Fig. 8 summarise the EPR parameters and evolution characteristics of PFRs in BACs during biomass pyrolysis.

It is worth noting that after pyrolysis, the powders were stored for 90 days before the first EPR characterisation. Then, they were reanalysed after 60 days, to confirm the good stability of PFRs, if not exposed to atmospheric oxygen. The broad single hyperfine signal was detected for B400, B500 and B600, establishing the formation of radicals in high concentration (around 10^{19} spins per g). At lower temperatures (B300), the thermal treatment was not enough for producing radical species, while at the highest temperatures (B700 and B800), the formed PFRs quenches during the carbon's polymerisation. As reported in the literature, *g*-factor < 2.0030 is characteristic of carbon-centred radicals, while carbon-centred radicals adjacent to oxygen atoms have *g*-factors ranging from 2.0030 to 2.0040. A *g*-value greater than 2.0040 indicates the presence of PFRs in oxygen-centred radicals. The increasing of pyrolysis temperature induces the transition of *g*-factor from 2.0036 to

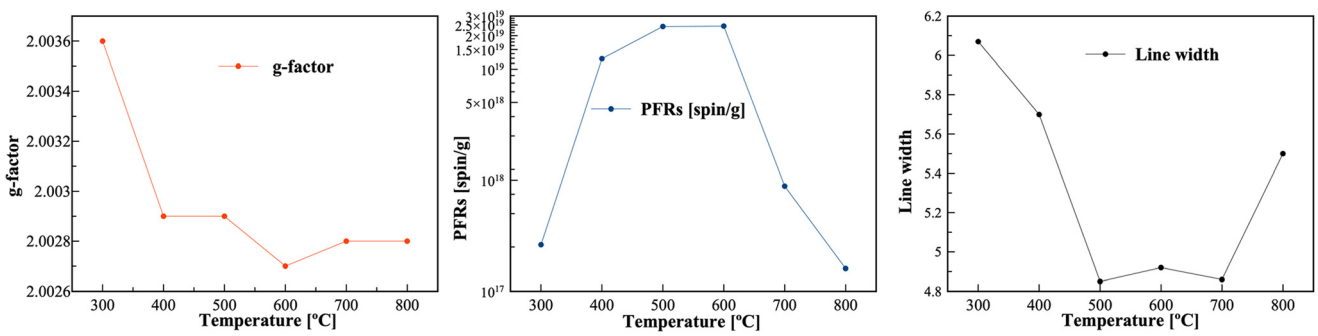

Fig. 8 EPR parameters *g*-factor (left), PFR concentration (centre), and line width (right) of BAC powders stored for 3 months under N_2 at +4 °C.

Table 8 Textural properties of the BAC powder ball-milled for 20 minutes, measured through N_2 adsorption/desorption at 77 K

Sample	Surface area [m^2 g^{-1}]	Total pore volume [cm^3 g^{-1}]	Micropore volume [cm^3 g^{-1}]	Mean pore size [nm]
B400	16.5	0.031	0	BET: 4.7/BJH: 11.4
B500	345.0	0.164	0.068	BET: 2.1/BJH: 3.9
B600	462.3	0.230	0.149	BJH: 1.8

2.0027, indicating the conversion of oxygen-centred radicals to carbon-centred radicals.

Table 8 summarizes the results of BET and BJH analysis, carried out to determine the specific surface area (S_{BET}), the total pore volume and the micropore volume for the B400, B500 and B600 samples. Measures were made through N_2 adsorption/desorption at 77 K (Fig. 9). These samples were those which presented the highest content of PFRs and were tested as a potential bio-adsorber for MB removal.

The pyrolysis temperature had a clear impact on the specific surface area of the BAC samples, which increased from 16.5 m^2 g^{-1} to 345 m^2 g^{-1}, raising the temperature from 400 °C to 500 °C. Upon a further increase up to 600 °C, the specific surface area reached about 462 m^2 g^{-1}. This trend can be easily visualized analysing the graph reported in Fig. 9, that shows the N_2 adsorption (solid) and desorption (dashed) isotherms registered for B400 (red), B500 (purple) and B600 (light blue) samples.

For all the samples tested, the desorption hysteresis never completely closed at 0.4 relative pressure. This phenomenon is well known for coals and biochar and is generally explained as a combination of two factors. First, the structure of amorphous carbon material is not rigid and can deform due to adsorption or pore filling.[44] Second, the surface affinity for nitrogen atoms hinders the release of gas molecules that remain trapped within the porous structure.[45]

The higher the surface area of the sample, the higher the specific quantity of N_2 adsorbed on the sample. Fig. 9 reports the cumulative pore volume for the BACs obtained at different temperatures. Despite having the largest surface area and pore volume of all the tested samples, B600 was almost completely characterised by micropores (pores <2 nm, as defined by IUPAC). Specifically, almost 65% of the total pore volume could be attributed to micropores that are not easily accessible by large molecules like methylene blue (1.45 × 0.95 × 0.40 nm).[46] Therefore, their contribution to the adsorption process could be negligible. The BAC prepared at a lower temperature showed a gradual increase of mesopore fraction (pores with a width of 2–50 nm as defined by IUPAC), accounting for almost 60% of the total pore volume of B500. Considering B400, the *t*-plot method confirmed the complete absence of micropores. The size of the cavities in the BAC sample fell within the range of mesopores and macropores that can be exploited for MB adsorption.

The morphology of all samples was relatively similar, with a broad particle size distribution, ranging from ~100 nm to a few microns (Fig. S3). While B500 and B600 could easily be imaged and were assumed to be excellent conductors, B400 suffered from charging under the electron beam, suggesting that the material was not fully graphitized. The particles present broken, cleaved edges and surfaces with visible roughness. As the fragments are small compared to the features of the virgin bamboo, no obvious micro-scale structure appears to be retained after the pyrolysis and ball milling steps. EDX revealed the presence of impurities around the 1 at% level of Mg, Si, K, Ca and Cu.

3.2 EPR spin-trapping method in batch or flow mode.

Theoretically, the BACs radicals R˙ reacted with H_2O_2 to produce transient hydroxyl radicals, ˙OH, according to the following reaction:

$$R^{\cdot} + H_2O_2 \rightarrow ROH + {}^{\cdot}OH$$

To directly evaluate the formation of ˙OH radicals caused by the PFRs present in the BACs' powders, an appropriate spin trap was used: 5,5-dimethyl-1-pyrroline *N*-Oxide (DMPO). The

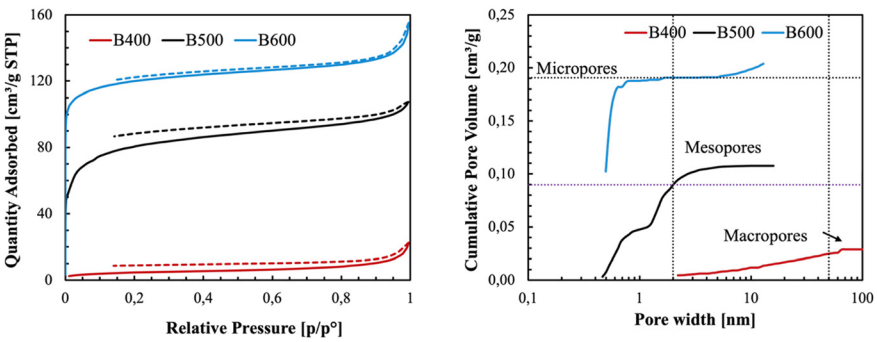

Fig. 9 (Left) N_2 adsorption (full lines) and desorption (dashed lines) isotherm for BAC (B400, B500 and B600). (Right) DFT analysis for cumulative pore volume of BAC.

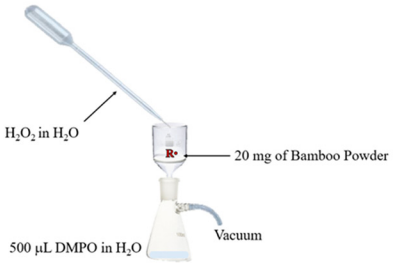

BAC powders	2nd Peak Intensity
B300	3.45E+04
B400	5.64E+04
B500	5.29E+04
B600	4.08E+04
B700	2.50E+04
B800	2.66E+04

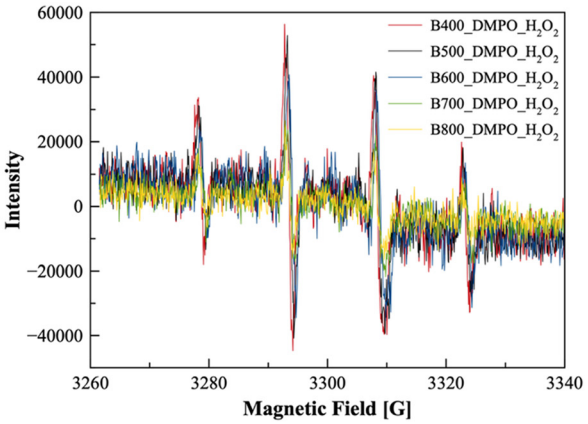

Fig. 10 Schematic illustration for generating stable paramagnetic DMPO˙–OH species with a sintered glass filter connected to the vacuum system. 20 mg of BAC were weighed into the sintered glass filter, and 500 µl of a diluted H_2O_2 (2.68 mM) was percolated through it and dropped directly inside a flask containing 0.02 M of DMPO. EPR spectra of DMPO˙–OH adducts in the final filtered solution (0.02 M of DMPO and 1.34 mM of H_2O_2, in H_2O) obtained from different BACs.

illustration in Fig. 10 depicts a glass vacuum filtration device used for the EPR-spin trap analysis, carried out for each different BAC. DMPO has been chosen as an ideal spin-trapping reagent to detect different ROS ($O_2^{\bullet-}$, HOO˙, ROO˙ and ˙OH) generating stable nitroxide radical characteristic of the trapped radical with an unambiguous EPR spectrum. To quantify the observed DMPO˙–OH spin-adduct, we considered the intensity of the second peak in the obtained spectra, as reported in the list inset in Fig. 10. As reported in Fig. 10, all the EPR experiments confirmed the reaction between the short-life transient radical (˙OH) with DMPO to produce a stable paramagnetic adduct (DMPO˙–OH) with four-line EPR spectra.

B400 had a lower spin per g of PFRs at solid-state (1.2×10^{19} spin per g), than B500 and B600, it produced a slightly higher amount of the stable spin-adduct DMPO–OH. These observations drove us to pack the chromatographic column with different amounts of B400 and B500 percolating into the bed-packed reactor the MB solutions. The different operational conditions are summarized in Table 1 and the removal percentage (% *R*) results are presented in Fig. 11.

A general observation over all the experiments shown in Fig. 11, comparing the removal efficiency of B400 and B500, leads us to assume that B400 is quantitatively better than B500. Considerations about B400 included: i) EPR spin-trap analysis determined a slightly higher concentration of the

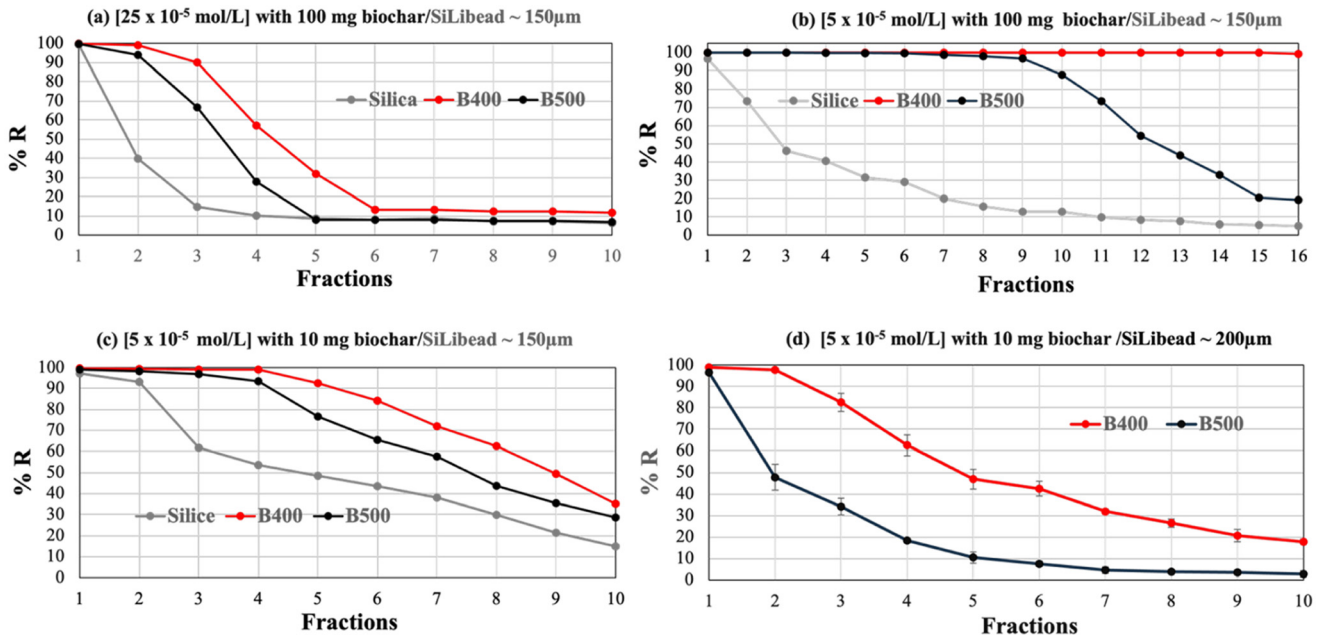

Fig. 11 Percentage removal (% *R*) of MB in different experimental conditions as reported in Table 1: type and mass of biochar, granulometry of SiLibeads® as supports, concentration and volume of MB solution are indicated in each panel.

Table 9 Maximum adsorption capacity (Ads_{max}) determination varying concentration and volume of MB solutions, and the amounts of the BAC used

MB [mol L^{-1}] and volume	B400 [mg]	SiLibeads® support	Ads_{max} [mg_{dye} $g_{biochar}^{-1}$]	
[25×10^{-5}] 100 mL	100	~150 μm	[a]12.7/[b]19.1	Fig. 11a
[5.0×10^{-5}] 100 mL	10	~150 μm	[c]24.4	Fig. 11c
[5.0×10^{-5}] 100 mL	10	~200 μm	[d]35.3	Fig. 11d

[a] Calculated considering the first 3 fractions (30 mL) with a % $R > 90\%$ and subtracted by the support's adsorption. [b] Calculated considering the first 5 fractions (50 mL) and subtracted from the support's adsorption. [c] Calculated considering the first 5 fractions (50 mL) with a % $R > 90\%$ and subtracted from the support's adsorption. [d] Calculated considering the first 2 fractions (20 mL) with a % $R > 90\%$ (the support's adsorption is less than 5%).

DMPO–OH adduct formed *in situ*; ii) the BET analysis confirmed the presence of mesopores and macropores accessible to large molecules like MB (1.45 × 0.95 × 0.40 nm); iii) IR and XPS spectroscopy attributed chemical functionalities, such as, hydroxyl, carbonylic and carboxylic groups useful to increase the adsorption of the organic dye onto the surface followed by the AOPs sustained by PFRs.

In Fig. 11a and b, fixing the mass of BAC at 100 mg, and decreasing the MB concentration from 25 to 5 × 10^{-5} mol L^{-1}, the increased removal efficiency of B400 was established. On the contrary, an overloading of the bed-packed reactor led to a saturation of the BAC, after three recollected fractions for a total of 30 mL of MB solution percolating into BAC-based bed reactor. Looking at Fig. 11b and c, fixing the concentration of MB solution at 5 × 10^{-5} mol L^{-1}, but decreasing the mass of the biochar from 100 to 10 mg, caused a clear fall of the removal efficiency with a maximum adsorption capacity (Ads_{max} for of 24.4 mg_{dye} g_{BAC}^{-1}). Finally, in Fig. 14d, we used a SiLibeads® with a granulometry around 200 μm only to avoid the interference of the support absorption, thus confirming the higher removal efficiency of B400 compared to B500, with an Ads_{max} of 35.3 mg_{dye} g_{BAC}^{-1}. In this case, BAC was ball-milled for 20 minutes, as in our previous work.[26] In Table 9, we notice that the Ads_{max} depended mainly on the operational conditions, thus making difficult to compare the results obtained in this work with those of other published batch experimental designs. Considering our previous work[26] in which we used an inactivated biochar (B400-N_2) in the same condition of Fig. 11d, Ads_{max} was of 19.1 mg_{dye} g_{BAC}^{-1}, and reached the value of 25.7 mg_{dye} g_{BAC}^{-1} by adding H_2O_2 with a molar ration MB/H_2O_2 = 1/50. This observation highlights the enhanced removal efficiency of BAC here reported, even without the presence of H_2O_2 to generate hydroxyl radicals.

To confirm these unprecedented results, we set up a long-term removal stability comparing B400, B400-H_2O_2, and B400-N_2 (no activated biochar), whose results have been reported in the following Fig. 12.

While we have demonstrated that BAC possesses a significantly higher performance than the non-activated counterpart, the addition of H_2O_2 to the activated B400 produced in this work did not enhance its removal efficiency, leading to the conclusion that hydrogen peroxide is not essential for the $^{\bullet}OH$ radical generation. Alternatively, we demonstrated that the reaction pathway to generate $^{\bullet}OH$ is determined by the molecular oxygen dissolved in solution. Fig. 13 shows the % R of three columns packed with fresh (red line) and aged B400 (purple and pink lines), varying the dissolved oxygen concentrations in the reservoir solution, continuously purging He (pink line) or air (purple line). Fig. 13 also shows that the removal efficiency loss over time of an aged B400 (black line) can be partially recovered by purging air (purple line).

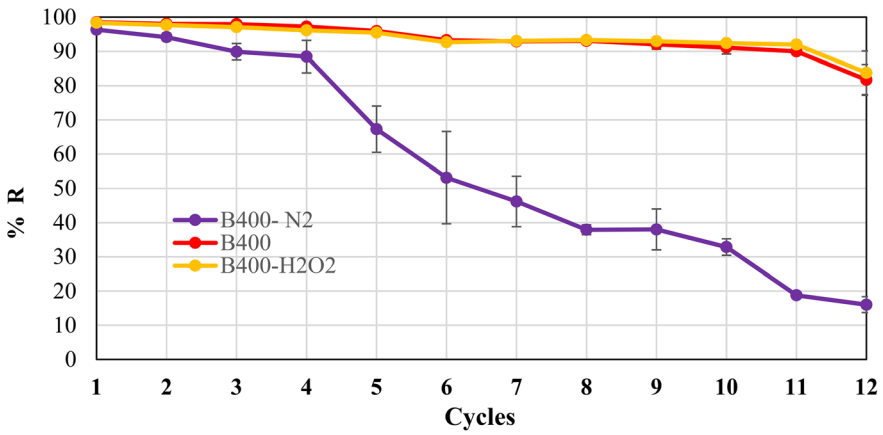

Fig. 12 Long-term removal stability (24 hours) in the removal efficiency of B400, B400-H_2O_2 and B400-N_2 (non-activated biochar). 10 mL MB solution was recycled for 2 hours-cycles for a total of 12 cycles (MB 2.5 × 10^{-5} mol L^{-1}).

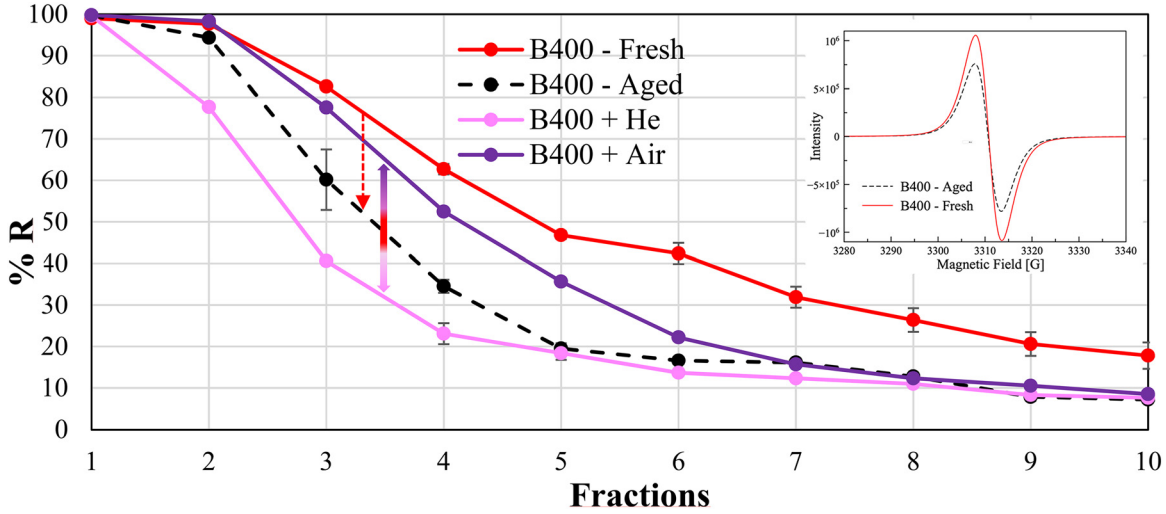

Fig. 13 % removal of MB in continuous flow (100 mL, 5×10^{-5} mol L^{-1}) of three column-packed systems with different concentrations of dissolved oxygen in contact with B400 : B400-fresh (red line); B400-aged (black dashed line); B400-insufflated He (pink line) and B400-insufflated with air (O_2) (purple line). The insert reports the EPR spectra of B400-fresh and B400-aged samples.

As we know, an aged B400 loses its removal efficiency more rapidly if compared to a recently prepared sample (named B400-fresh), as evidenced by the PFRs decreasing in the inset EPRs spectra. But this study demonstrated for the first time that it is possible to recover part of the lost BAC performance simply by bubbling air into the MB solution, thus enriching the amount of O_2 necessary to generate $^{\bullet}OH$. Conversely, we demonstrated that bubbling He in the system, thus minimizing the dissolved O_2 in the solution, resulted in a dramatic decrease in the % R against MB. EPR analysis, in batch and flow mode, demonstrates the relevant role of molecular oxygen in forming $^{\bullet}OH$. Following a procedure reported in the section 2.2, EPR spin-trap analyses were carried out, whose results are reported in Table 10 and Fig. 14. In the B400 suspension purged with air, the DMPO$^{\bullet}$–OH adduct had one order of magnitude higher than the purged N_2 sample.

Fig. 14 (right) shows the EPR spectra of the DMPO$^{\bullet}$–OH spin adduct observed in the vial containing buffered DMPO in which the H_2O (purged with N_2 and air) was dropped directly after percolation through a B400-based bed-packed column. The DMPO$^{\bullet}$–OH EPR signal generated by the water purged with N_2 was almost 60% lower than that observed upon purging with air (enriched O_2). Considering the flow rate injection at 250 μL min^{-1}, and a micrometric tube (ϕ = 100 μm, L = 300 mm, V = 0.0047 mL) connection from the column to the vial, it is worth noticing that the more stable ROS ($O_2^{\bullet-}$, H_2O_2) formed during the process, survived more than 1.13 seconds (resident time). The unstable hydroxyl radical ($^{\bullet}OH$) produced from the more stable ROS was trapped in the vial containing the DMPO spin-trap, confirmed by the EPR four-line signal. These findings substantiate the capacity of PFRs to produce hydroxyl radicals in the presence of oxygen, without the addition of external chemical oxidants.

Table 10 EPR analysis of the DMPO$^{\bullet}$–OH generation by B400 suspensions and B400 in a packed flow system, purging N_2 and air into the reservoir solution with its schematic illustration

Batch *vs.* flow	Gas in water	2nd peak intensity
B400 in suspension	Purging N_2	4.55×10^4
	Purging air	1.56×10^5
B400 in packed column	Purging N_2	1.07×10^5
	Purging air	2.80×10^5

Kinetic study. Fig. S4 in Section S3 in SI are derived by a modification of Fig. 13, not considering the dotted line, where cycles were substituted with the corresponding times. It evidences that, for three columns-packed adsorbent/degradation systems filled with B400 or B400 and insufflated with either He or O_2 during all process, the first two hours of work in continuous flux, were sufficient to reach the maximum of MB removal percentage (% R) (99.7, 99.6 and 99.8%, respectively). Further work, up to 20 hours in continuous flux, determined a gradual removal capacity loss (% RL), whose rate depended on the working conditions, until a minimum removal percentage of 7.2 (B400), 7.6 (B400 + He) and 8.5% (B400 + O_2) (Fig. S4).

Removal processes of pollutant chemical species have high importance in several industries, therefore, it is crucial to investigate the absorption/degradation efficiency of adsorbents, as well as their loss of absorption/degradation efficiency over time from kinetics perspectives. In this regard, many researchers are actively engaged in presenting various studies on such removal processes for different substances captured on several absorbent surfaces, to accurately establish the main mechanisms governing them.[47–49] Adsorption/degradation kinetic models can provide a framework for predicting mass and surface diffusion, adsorption/degradation rate constants, and are instrumental

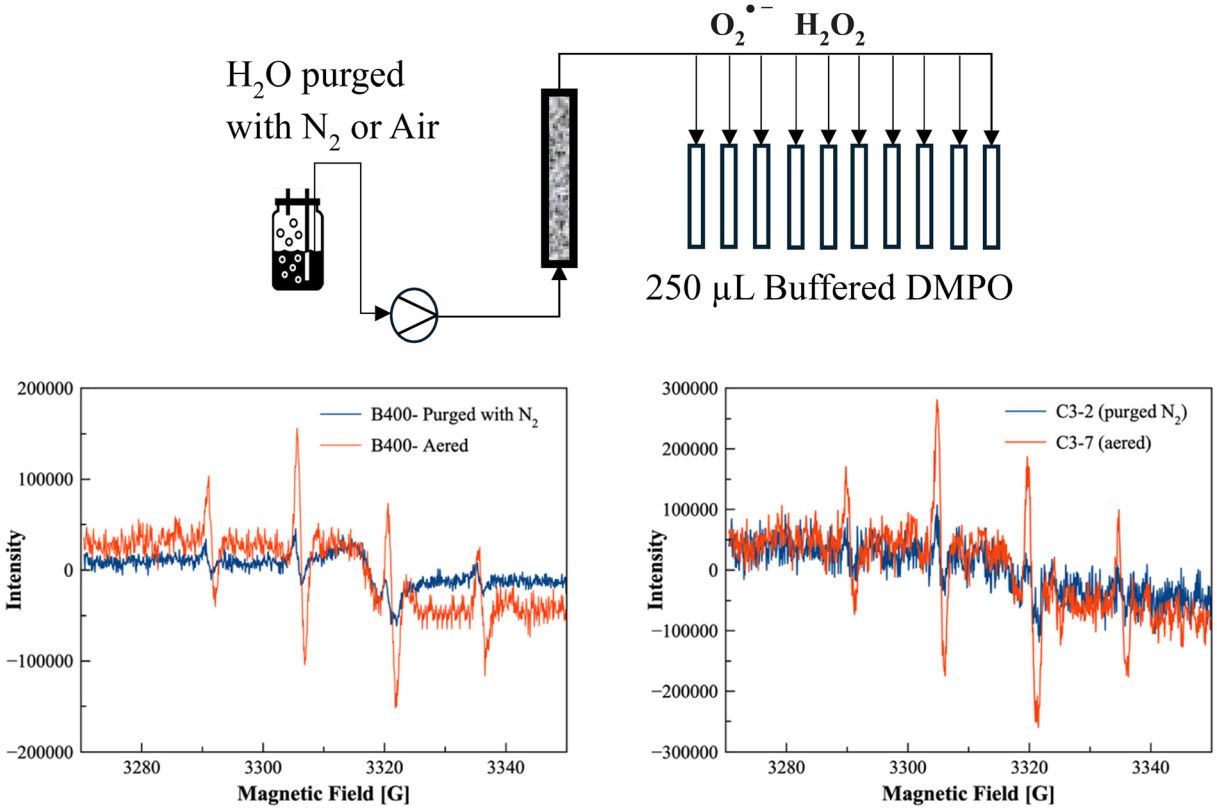

Fig. 14 (Left) EPR spectra of DMPO˙–OH generated into B400 suspensions aerated and not, batch mode. (Right) EPR spectra of DMPO˙–OH generated in the vial containing DMPO solution and the purged water percolated through a B400-based bed-packed column dropped into it.

in elucidating the dynamics of adsorption/degradation processes.[47] Here, the kinetic models reported in Table 2 have been used to study the data of adsorption/degradation efficiency loss (%) over time reported in Fig. S4. Fig. S5–S10 show the dispersion graphs (indicators without lines) obtained for the six models used and the related linear regression lines (dotted lines with the same colour of the indicators) with their equations and the coefficients of determination (R^2) values. The linear regressions and their equations were provided by Microsoft Excel software 365 using the ordinary least square (OLS) method. R^2 values associated with all the equations in Fig. S5–S10 have been reported in Table S1 and were considered as the parameters to determine which model best fit the % R data according to the literature.[50] R^2 values obtained for the linear regression lines of all tested kinetic models included in Table S1 evidenced that the MB % RL over time (20 hours of work in continuous flux) of all the systems best fit FO kinetics (R^2 = 0.9807, 0.9833 and 0.9693). Moreover, the B400 + He and B400 + O_2 systems well fit also with the PFO (R^2 = 0.9645 and 0.9629), while B400 + He demonstrated a well fit also with Korsmeyer–Peppas kinetic model (R^2 = 0.9694).

The FO and PFO kinetic models are approaches widely used for analysing adsorption data concerning the adsorption of adsorbates from gaseous as well as solution phases. When applied to data of absorption/degradation efficiency over time up to an equilibrium, they describe the rate of adsorption/degradation, which is proportional to the number of unoccupied binding sites on adsorbents or to the chemical species promoting pollutants degradation, if present.[51] Applied to our data of MB % RL over a time of 20-hours working in continuous flux, it can describe the rate of % RL, which can be due both to the saturation of absorbent no longer capable to retain additional adsorbate and to the decay of chemical species supporting the pollutant degradation, if present. In our recent work, we have demonstrated that the removal of MB from aqueous solutions occurs both by physisorption and by the oxidative degradation promoted by the presence of persistent free radicals (PFRs).[50] Moreover, it has been reported that the generation of hydroxyl radicals, which are the main responsible of the oxidative degradation of pollutants, starts with an electron transfer from PFRs to molecular oxygen to form superoxide radical ion. Then hydrogen peroxide and hydroxyl radicals can form *via* dismutation and Fenton reactions, respectively, thus establishing the essential role of oxygen in the removal processes.[52] Rationally, the addition of further O_2 in biochar-based removal systems containing PFRs during the removal process could increase their pollutants removal efficiency by oxidative degradation, due to a higher concentration of hydroxyl radicals and slow down their removal efficiency loss rate over time. Since all the systems best fitted with the FO kinetics and B400 + He and B400 + O_2 fitted well also with PFO ones, it can be assumed that their

rate of % RL over time can depend both on the absence of further unoccupied binding sites on adsorbents and on the decay of PFRs and consequently on the decrease of hydroxyl radicals. From profiles in Fig. S4, the rate of MB removal efficiency loss resulted slower in the B400 + O_2 system than in the B400, because of the presence of a higher concentration of hydroxyls radicals due to the major content of O_2, thus confirming that MB removal by these systems occurs by both adsorption and oxidative degradation promoted by PFRs. Concerning B400 + He, because of the total absence of O_2, and therefore of the very low concentration of hydroxyl radicals, due to the flux of He, the MB % RL resulted faster, thus confirming that MB removal by this system occurs mainly by adsorption and in minor extent by the oxidative degradation promoted by PFRs.

Moreover, the system made of B400 + He best fitted also the Korsmeyer–Peppas model. Such model establishes that the main mechanisms for pollutants removal efficiency and therefore for the % RL over time could be diffusional or governed by more complex not chemical processes (case II or super case II transport) depending on the value of the diffusional or transport exponent n_{KP}.[53] Specifically, $n \leq 0.45$ corresponds to a Fickian diffusion mechanism, $0.45 < n < 0.89$ to non-Fickian transport, $n = 0.89$ to case II (relaxational) transport, and $n > 0.89$ to super case II transport.[54,55] In all cases, the fact that Korsmeyer–Peppas model fit well with data of B400 + He confirmed that, due to the absence of O_2 and paucity of hydroxyl radicals, its MB removal efficiency depended scarcely on chemical processes and oxidative degradation reactions, but mainly on diffusional absorption, thus making faster its removal efficiency loss (%) over time. Table S2 SI contains important kinetic parameters of FO, PFO and Korsmeyer–Peppas models calculated according to literature from the equations reported in the Fig. S5, S6 and S10.[50,56,57] In this regard, K_1 values confirmed that the highest rate of % RL was that of B400 + He system, due to the absence of O_2 and very low concentrations of hydroxyl radicals, not supporting MB removal. On the contrary, the slowest rate of % RL was that of B400 + O_2 system, where the high concentration of O_2 and then of hydroxyls radicals, supported better and for longer times the MB removal. B400 system not containing additional O_2 and possessing limited concentration of hydroxyls radicals showed a rate of % RL lower than that of B400 + He, but higher than that of B400 + O_2 system. The same results were derived by considering the PFO kinetic models' rate constants. Concerning n_{KP} value obtained for B400 + He system, it was >0.89 thus establishing that complex super case II transport not chemical mechanisms mainly governed its removal process. Using a modified version of FO kinetic model, obtained without imposing the intercept equal to zero, the % R (RE% in Table S3), at equilibrium, predicted by the model, *i.e.* after 20 hours of work in continuous flux, was calculated for all systems, inserted in columns 3 of Table S2 and compared with experimental ones. All calculated values of the % *R* (RE% in Table S3) using the equations of models significantly differed from experimental ones for both B400, B400 + He and B400 + O_2 systems. Anyway, such values confirmed that the more efficient system was the B400 + O_2 followed by the B400 and then by the B400 + He one, based on the concentration of oxygen and therefore hydroxyl radicals supporting the MB oxidative degradation.

A similar study, detailed in SI (Fig. S11–S17 and Tables S3 and S4), was performed on data of % RL over 240 minutes of working in continuous flux of different removal systems made of columns filled with biochar prepared using different pyrolysis conditions (400 °C under N_2 or 400 °C under N_2 + CO_2). The biochar obtained in the second condition was used in absence or in presence of H_2O_2 during the removal process (Fig. S11). The experiment was monitored by UV-vis spectroscopy, analysing the MB solution passed in continuous flux in columns at fixed time points (cycles in Fig. 12) of 20 minutes each one.

4. Conclusion

The study highlighted the role of permanent free radicals (PFRs) in generating hydroxyl radicals (˙OH) in the presence of dissolved oxygen. This finding could lead to the development of new AOPs that do not require external chemical oxidants, making the process more cost-effective and environmentally friendly.

The bamboo activated carbon (BAC) production process involved heating bamboo at high temperatures in an oxygen-limited environment, followed by activation with CO_2. The results demonstrated that the activated biochar exhibited high efficiency in MB removal, significantly influenced by the concentration and stability of PFRs, which have been monitored for 5 months. Two sets of experiments have been carried out to discriminate the path reaction of hydroxyl radical generation operated by PFR and the role of O_2 or H_2O_2 in forming ROS. The addition of H_2O_2 did not increase the MB removal performance of the activated biochar. Continuously bubbling air, the increased molecular oxygen in the MB solution enhanced the removal efficiency of aged B400, almost recovering the performance of the fresh B400. BAC's adsorption capacity reached a value of 34 mg g^{-1}, superior to that of non-activated biochar without adding chemical oxidant to produce reactive oxygen species. The mathematical models best fitting the data of removal efficiency loss (%) over time confirmed the pivotal role of PFRs, O_2 and hydroxyl radicals in the removal of MB, which occurred by both adsorption and AOPs. Moreover, kinetic studies and kinetic constants by different models evidenced that the rate of removal efficiency loos overtime was unequivocally lower when BAC with addition of O_2 was used, thus further confirming that oxygen and the hydroxyl radicals' continuous production by the action of PFRs on O_2 are essential for an efficient removal of MB by AOPs.

The insights gained from this study could be applied to other types of organic pollutants beyond methylene blue. The

ability of BACs to generate ROS *in situ* suggests potential applications in the degradation of various organic contaminants in water. By eliminating the need for additional chemical oxidants, the use of BACs in wastewater treatment could reduce operational costs and simplify the treatment process. This makes the technology more accessible and practical for widespread adoption, particularly in regions with limited resources.

Author contributions

Author Contributions: Paola Franchi, Anna Turchetti and Marco Lucarini performed EPR measurements; Adolfo Manucci and Alessandro Pellis prepared the samples and performed Organic dye removal studies; Marcello Pagliero and Antonio Comite performed the BET and BJH analysis; Letizia Savio and Elina Mkrtchian performed XPS measurements; Giorgio Divitini and Ambra Celotto performed SEM and EDX measurements, Sergio Marras performed XRD measurements; Tommaso Del Rosso and Sidnei Paciornik performed FT-ATR, DRIFTS and Raman measurements. Silvana Alfei performed the Kinetic studies; Sidnei Paciornik and Omar Ginoble Pandoli are responsible for the conceptualisation of the work, project administration and funding acquisition. All the co-authors contributed to the original draft preparation, review and editing of the final manuscript.

Conflicts of interest

The authors declare no conflicts of interest.

Data availability

Supplementary information: XRD pattern, SEM analysis and kinetic studies. See DOI: **https://doi.org/10.1039/D5CY00632E**.

The data supporting this article have been included as part of the SI.

Acknowledgements

This work was funded with financial support of Fundação Carlos Chagas Filho Amparo à Pesquisa do Estado do Rio de Janeiro (FAPERJ) (SEI-260003/001227/2020), Coordenação de Aperfeiçoamento de Pessoal de Nível Superior – Brasil (CAPES) – Finance Code 001. We acknowledge financial support under the National Recovery and Resilience Plan (NRRP), Mission 4, Component 2, Investment 1.1, Call for tender No. 104 published on 2.2.2022 by the Italian Ministry of University and Research (MUR), funded by the European Union – NextGenerationEU– Project Title SUSTCARB – CUP D53D23010360006, – Grant Assignment Decree No. 1064 adopted on July 18, 2023, by the Italian Ministry of Ministry of University and Research (MUR). LS acknowledges funding from the European Union – NextGenerationEU, Mission 4, Component 1, through the Italian Ministry of University and Research under project PRIN-PNRR P20227XSAH, CUP B53D23028390001. Open Access publishing facilitated by the Università degli Studi di Genova, as part of the CRUI-CARE agreement. We thank Silvia Dante for the Raman analysis.

References

1 S. Alfei and O. G. Pandoli, Bamboo-Based Biochar: A Still Too Little-Studied Black Gold and Its Current Applications, *J. Xenobiot.*, 2024, **14**, 416–451, DOI: **10.3390/jox14010026**.

2 S. Alfei and O. G. Pandoli, Biochar-Derived Persistent Free Radicals: A Plethora of Environmental Applications in a Light and Shadows Scenario, *Toxics*, 2024, **12**, 245, DOI: **10.3390/toxics12040245**.

3 R. Zhang, R. Zhang, A. R. Zimmerman, H. Wang and B. Gao, Applications, impacts, and management of biochar persistent free radicals: A review, *Environ. Pollut.*, 2023, **327**, 121543, DOI: **10.1016/j.envpol.2023.121543**.

4 E. S. Odinga, M. G. Waigi, F. O. Gudda, J. Wang, B. Yang, X. Hu, S. Li and Y. Gao, Occurrence, formation, environmental fate and risks of environmentally persistent free radicals in biochars, *Environ. Int.*, 2020, **134**, 105172, DOI: **10.1016/j.envint.2019.105172**.

5 E. P. Vejerano, G. Rao, L. Khachatryan, S. A. Cormier and S. Lomnicki, Environmentally Persistent Free Radicals: Insights on a New Class of Pollutants, *Environ. Sci. Technol.*, 2018, **52**, 2468–2481, DOI: **10.1021/acs.est.7b04439**.

6 Y. Wang, X. Gu, Y. Huang, Z. Ding, Y. Chen and X. Hu, Insight into biomass feedstock on formation of biochar-bound environmentally persistent free radicals under different pyrolysis temperatures, *RSC Adv.*, 2022, **12**, 19318–19326, DOI: **10.1039/d2ra03052g**.

7 W. Tao, P. Zhang, H. Li, Q. Yang, P. Oleszczuk and B. Pan, Generation Mechanism of Persistent Free Radicals in Lignocellulose-Derived Biochar: Roles of Reducible Carbonyls, *Environ. Sci. Technol.*, 2022, **56**, 10638–10645, DOI: **10.1021/acs.est.1c06997**.

8 D. Chen, J. Xu, P. Ling, Z. Fang, Q. Ren, K. Xu, L. Jiang, Y. Wang, S. Su, S. Hu and J. Xiang, Formation and evolution mechanism of persistent free radicals in biochar during biomass pyrolysis: Insights from biochar's element composition and chemical structure, *Fuel*, 2024, **357**, 129910, DOI: **10.1016/j.fuel.2023.129910**.

9 X. Xiao, B. Chen, Z. Chen, L. Zhu and J. L. Schnoor, Insight into Multiple and Multilevel Structures of Biochars and Their Potential Environmental Applications: A Critical Review, *Environ. Sci. Technol.*, 2018, **52**, 5027–5047, DOI: **10.1021/acs.est.7b06487**.

10 K. Luo, Y. Pang, D. Wang, X. Li, L. Wang, M. Lei, Q. Huang and Q. Yang, A critical review on the application of biochar in environmental pollution remediation: Role of persistent free radicals (PFRs), *J. Environ. Sci.*, 2021, **108**, 201–216, DOI: **10.1016/j.jes.2021.02.021**.

11 M. F. Gasim, Z. Y. Choong, P. L. Koo, S. C. Low, M. H. Abdurahman, Y. C. Ho, M. Mohamad, I. W. K. Suryawan, J. W. Lim and W. Da Oh, Application of Biochar as Functional Material for Remediation of Organic Pollutants

in Water: An Overview, *Catalysts*, 2022, **12**(2), 210, DOI: **10.3390/catal12020210**.

12 Z. Kang, X. Jia, Y. Zhang, X. Kang, M. Ge, D. Liu, C. Wang and Z. He, A Review on Application of Biochar in the Removal of Pharmaceutical Pollutants through Adsorption and Persulfate-Based AOPs, *Sustainability*, 2022, **14**(16), 10128, DOI: **10.3390/su141610128**.

13 X. Ruan, Y. Sun, W. Du, Y. Tang, Q. Liu, Z. Zhang, W. Doherty, R. L. Frost, G. Qian and D. C. W. Tsang, Formation, characteristics, and applications of environmentally persistent free radicals in biochars: A review, *Bioresour. Technol.*, 2019, **281**, 457–468, DOI: **10.1016/j.biortech.2019.02.105**.

14 Y. Yuan, N. Bolan, A. Prévoteau, M. Vithanage, J. K. Biswas, Y. S. Ok and H. Wang, Applications of biochar in redox-mediated reactions, *Bioresour. Technol.*, 2017, **246**, 271–281, DOI: **10.1016/j.biortech.2017.06.154**.

15 X. Zhou, Y. Zhu, Q. Niu, G. Zeng, C. Lai, S. Liu, D. Huang, L. Qin, X. Liu, B. Li, H. Yi, Y. Fu, L. Li, M. Zhang, C. Zhou and J. Liu, New notion of biochar: A review on the mechanism of biochar applications in advannced oxidation processes, *Chem. Eng. J.*, 2021, **416**, 129027, DOI: **10.1016/j.cej.2021.129027**.

16 Faheem, J. Du and S. H. Kim, *et al.*, Application of biochar in advanced oxidation processes: supportive, adsorptive, and catalytic role, *Environ. Sci. Pollut. Res.*, 2020, **27**, 37286–37312.

17 H. Jiang, H. Chen, Z. Duan, Z. Huang and K. Wei, Research progress and trends of biochar in the field of wastewater treatment by electrochemical advanced oxidation processes (EAOPs): a bibliometric analysis, *J. Hazard. Mater. Adv.*, 2023, **10**, 100305, DOI: **10.1016/j.hazadv.2023.100305**.

18 M. Aeschbacher, M. Sander and R. P. Schwarzenbach, Novel electrochemical approach to assess the redox properties of humic substances, *Environ. Sci. Technol.*, 2010, **44**, 87–93, DOI: **10.1021/es902627p**.

19 F. J. Chacón, M. L. Cayuela, A. Roig and M. A. Sánchez-Monedero, Understanding, measuring and tuning the electrochemical properties of biochar for environmental applications, *Rev. Environ. Sci. Bio/Technol.*, 2017, **16**, 695–715, DOI: **10.1007/s11157-017-9450-1**.

20 A. Prévoteau, F. Ronsse, I. Cid, P. Boeckx and K. Rabaey, The electron donating capacity of biochar is dramatically underestimated, *Sci. Rep.*, 2016, **6**(1), 32870, DOI: **10.1038/srep32870**.

21 J. Yuan, Y. Wen, D. D. Dionysiou, V. K. Sharma and X. Ma, Biochar as a novel carbon-negative electron source and mediator: electron exchange capacity (EEC) and environmentally persistent free radicals (EPFRs): a review, *Chem. Eng. J.*, 2022, **429**, 132313, DOI: **10.1016/j.cej.2021.132313**.

22 T. Wang, Z. Zhang, Z. Gu, C. Hu and J. Qu, Electron Transfer of Activated Carbon to Anode Excites and Regulates Desalination in Flow Electrode Capacitive Deionization, *Environ. Sci. Technol.*, 2023, **57**, 2566–2574, DOI: **10.1021/acs.est.2c09506**.

23 A. Schievano, R. Berenguer, A. Goglio, S. Bocchi, S. Marzorati, L. Rago, R. O. Louro, C. M. Paquete and A. Esteve-Núñez, Electroactive Biochar for Large-Scale Environmental Applications of Microbial Electrochemistry, *ACS Sustainable Chem. Eng.*, 2019, **7**, 18198–18212, DOI: **10.1021/acssuschemeng.9b04229**.

24 L. Klüpfel, M. Keiluweit, M. Kleber and M. Sander, Redox properties of plant biomass-derived black carbon (biochar), *Environ. Sci. Technol.*, 2014, **48**, 5601–5611, DOI: **10.1021/es500906d**.

25 G. Fang, C. Zhu, D. D. Dionysiou, J. Gao and D. Zhou, Mechanism of hydroxyl radical generation from biochar suspensions: Implications to diethyl phthalate degradation, *Bioresour. Technol.*, 2015, **176**, 210–217, DOI: **10.1016/j.biortech.2014.11.032**.

26 F. Zanardi, F. Romei, M. N. B. Junior, S. Paciornik, P. Franchi, M. Lucarini, A. Turchetti, L. Poletti, S. Alfei and O. G. Pandoli, Pivotal Contribute of EPR-Characterized Persistent Free Radicals in the Methylene Blue Removal by a Bamboo-Based Biochar-Packed Column Flow System, *ChemCatChem*, 2024, **16**, 21, DOI: **10.1002/cctc.202401042**.

27 G. Fang, J. Gao, C. Liu, D. D. Dionysiou, Y. Wang and D. Zhou, Key role of persistent free radicals in hydrogen peroxide activation by biochar: Implications to organic contaminant degradation, *Environ. Sci. Technol.*, 2014, **48**, 1902–1910, DOI: **10.1021/es4048126**.

28 L. Khachatryan, E. Vejerano, S. Lomnicki and B. Dellinger, Environmentally persistent free radicals (EPFRs). 1. Generation of reactive oxygen species in aqueous solutions, *Environ. Sci. Technol.*, 2011, **45**, 8559–8566, DOI: **10.1021/es201309c**.

29 M. J. Barbosa Nogueira, S. Chauque, V. Sperati, L. Savio, G. Divitini, L. Pasquale, S. Marras, P. Franchi, S. Paciornik, R. Proietti Zaccaria and O. Ginoble Pandoli, Untreated bamboo biochar as anode material for sustainable lithium ion batteries, *Biomass Bioenergy*, 2025, **193**, 107511, DOI: **10.1016/j.biombioe.2024.107511**.

30 L. O. L. Gontijo, M. N. Barbosa Junior, D. Santos de Sá, S. Letichevsky, M. J. Pedrozo-Peñafiel, R. Q. Aucélio, I. S. Bott, H. Diniz Lopes Alves, B. Fragneaud, I. Oliveira, A. Linhares, L. Savio, G. Carraro, D. Anja, F. Lazaro, G. Khosrow, S. Paciornik and O. Ginoble, 3D conductive monolithic carbons from pyrolyzed bamboo for microfluidic self-heating system, *Carbon*, 2023, 118214, DOI: **10.1016/j.carbon.2023.118214**.

31 F. Meng, Y. Yu, Y. Zhang, W. Yu and J. Gao, Surface chemical composition analysis of heat-treated bamboo, *Appl. Surf. Sci.*, 2016, **371**, 383–390, DOI: **10.1016/j.apsusc.2016.03.015**.

32 H. Yu, C. Gui, Y. Ji, X. Li, F. Rao, W. Huan and L. Li, Changes in Chemical and Thermal Properties of Bamboo after Delignification Treatment, *Polymers*, 2022, **14**, 2573, DOI: **10.3390/polym14132573**.

33 A. Nikitin, L.-Å. Näslund, Z. Zhang and A. Nilsson, C–H bond formation at the graphite surface studied with core level spectroscopy, *Surf. Sci.*, 2008, **602**, 2575–2580, DOI: **10.1016/j.susc.2008.06.012**.

34 J. F. Moulder, J. Chastain and R. C. King, *Handbook of X-Ray Photoelectron Spectroscopy: A Reference Book of Standard Spectra for Identification and Interpretation of XPS Data*, 1995.

35 S. Alfei, B. Marengo, G. Zuccari, F. Turrini and C. Domenicotti, Dendrimer Nanodevices and Gallic Acid as Novel Strategies to Fight Chemoresistance in Neuroblastoma Cells, *Nanomaterials*, 2020, **10**, 1243, DOI: **10.3390/nano10061243**.

36 S. Kloss, F. Zehetner, A. Dellantonio, R. Hamid, F. Ottner, V. Liedtke, M. Schwanninger, M. H. Gerzabek and G. Soja, Characterization of Slow Pyrolysis Biochars: Effects of Feedstocks and Pyrolysis Temperature on Biochar Properties, *J. Environ. Qual.*, 2012, **41**, 990–1000, DOI: **10.2134/jeq2011.0070**.

37 V. Siipola, T. Tamminen, A. Källi, R. Lahti, H. Romar, K. Rasa, R. Keskinen, J. Hyväluoma, M. Hannula and H. Wikberg, Effects of biomass type, carbonization process, and activation method on the properties of bio-based activated carbons, *BioRes.*, 2018, **13**(3), 5976–6002, DOI: **10.15376/biores.13.3.5976-6002**.

38 S. Ramola, T. Mishra, G. Rana and R. K. Srivastava, Characterization and pollutant removal efficiency of biochar derived from baggase, bamboo and tyre, *Environ. Monit. Assess.*, 2014, **186**, 9023–9039, DOI: **10.1007/s10661-014-4062-5**.

39 D. Özçimen and A. Ersoy-Meriçboyu, Characterization of biochar and bio-oil samples obtained from carbonization of various biomass materials, *Renewable Energy*, 2010, **35**, 1319–1324, DOI: **10.1016/j.renene.2009.11.042**.

40 J. Coates, Interpretation of Infrared Spectra, A Practical Approach, *Encyclopedia of Analytical Chemistry*, John Wiley & Sons Ltd, 2000, pp. 10815–10837.

41 M. Fan, C. Li, Y. Sun, L. Zhang, S. Zhang and X. Hu, In situ characterization of functional groups of biochar in pyrolysis of cellulose, *Sci. Total Environ.*, 2021, **799**, 149354, DOI: **10.1016/j.scitotenv.2021.149354**.

42 M. Sevilla, P. Valle-Vigõn and A. B. Fuertes, N-doped polypyrrole-based porous carbons for CO2 capture, *Adv. Funct. Mater.*, 2011, **21**, 2781–2787, DOI: **10.1002/adfm.201100291**.

43 Z. Liu, Z. Du, W. Xing and Z. Yan, Facial synthesis of N-doped microporous carbon derived from urea furfural resin with high CO2 capture capacity, *Mater. Lett.*, 2014, **117**, 273–275, DOI: **10.1016/j.matlet.2013.12.021**.

44 Y. Cai, D. Liu, Z. Pan, Y. Yao, J. Li and Y. Qiu, Pore structure and its impact on CH4 adsorption capacity and flow capability of bituminous and subbituminous coals from Northeast China, *Fuel*, 2013, **103**, 258–268, DOI: **10.1016/j.fuel.2012.06.055**.

45 L. Qi, X. Tang, Z. Wang and X. Peng, Pore characterization of different types of coal from coal and gas outburst disaster sites using low temperature nitrogen adsorption approach, *Int. J. Min. Sci. Technol.*, 2017, **27**, 371–377, DOI: **10.1016/j.ijmst.2017.01.005**.

46 J. O. Ighalo, K. O. Iwuozor, C. A. Igwegbe and A. G. Adeniyi, Verification of pore size effect on aqueous-phase adsorption kinetics: A case study of methylene blue, *Colloids Surf., A*, 2021, **626**, 127119, DOI: **10.1016/j.colsurfa.2021.127119**.

47 J. Wang and X. Guo, Adsorption kinetic models: Physical meanings, applications, and solving methods, *J. Hazard. Mater.*, 2020, **390**, 122156, DOI: **10.1016/j.jhazmat.2020.122156**.

48 R. Ezzati, Adsorption kinetics at the solid/solution interface: Statistical Rate Theory (SRT) at close to equilibrium, *Surf. Interfaces*, 2017, **8**, 154–157, DOI: **10.1016/j.surfin.2017.05.010**.

49 S. Azizian, Kinetic models of sorption: a theoretical analysis, *J. Colloid Interface Sci.*, 2004, **276**, 47–52, DOI: **10.1016/j.jcis.2004.03.048**.

50 F. Zanardi, F. Romei, M. N. B. Junior, S. Paciornik, P. Franchi, M. Lucarini, A. Turchetti, L. Poletti, S. Alfei and O. G. Pandoli, Pivotal Contribute of EPR-Characterized Persistent Free Radicals in the Methylene Blue Removal by a Bamboo-Based Biochar-Packed Column Flow System, *ChemCatChem*, 2024, **16**, 21, DOI: **10.1002/cctc.202401042**.

51 E. D. Revellame, D. L. Fortela, W. Sharp, R. Hernandez and M. E. Zappi, Adsorption kinetic modeling using pseudo-first order and pseudo-second order rate laws: A review, *Clean. Eng. Technol.*, 2020, **1**, 100032, DOI: **10.1016/j.clet.2020.100032**.

52 L. Khachatryan, E. Vejerano, S. Lomnicki and B. Dellinger, Environmentally Persistent Free Radicals (EPFRs). 1. Generation of Reactive Oxygen Species in Aqueous Solutions, *Environ. Sci. Technol.*, 2011, **45**, 8559–8566, DOI: **10.1021/es201309c**.

53 I. Y. Wu, S. Bala, N. Škalko-Basnet and M. P. di Cagno, Interpreting non-linear drug diffusion data: Utilizing Korsmeyer-Peppas model to study drug release from liposomes, *Eur. J. Pharm. Sci.*, 2019, **138**, 105026, DOI: **10.1016/j.ejps.2019.105026**.

54 J. Siepmann, Modeling of drug release from delivery systems based on hydroxypropyl methylcellulose (HPMC), *Adv. Drug Delivery Rev.*, 2001, **48**, 139–157, DOI: **10.1016/S0169-409X(01)00112-0**.

55 P. L. Ritger and N. A. Peppas, A simple equation for description of solute release II. Fickian and anomalous release from swellable devices, *J. Controlled Release*, 1987, **5**, 37–42, DOI: **10.1016/0168-3659(87)90035-6**.

56 S. Alfei, V. Orlandi, F. Grasso, R. Boggia and G. Zuccari, Cationic Polystyrene-Based Hydrogels: Low-Cost and Regenerable Adsorbents to Electrostatically Remove Nitrites from Water, *Toxics*, 2023, **11**, 312, DOI: **10.3390/toxics11040312**.

57 S. Alfei, F. Grasso, V. Orlandi, E. Russo, R. Boggia and G. Zuccari, Cationic Polystyrene-Based Hydrogels as Efficient Adsorbents to Remove Methyl Orange and Fluorescein Dye Pollutants from Industrial Wastewater, *Int. J. Mol. Sci.*, 2023, **24**, 2948, DOI: **10.3390/ijms24032948**.